NASA CR-187103

NASA

ADVANCED ELECTRIC PROPULSION RESEARCH - 1990

Prepared for

LEWIS RESEARCH CENTER

NATIONAL AERONAUTICS AND SPACE ADMINISTRATION

Grant NGR-06-002-112

Annual Report

Jeffery M. Monheiser

May 1991

Approved by

Paul J. Wilbur
Department of Mechanical Engineering
Colorado State University
Fort Collins, Colorado 80523

NASA
National Aeronautics and Space Administration

Report Documentation Page

1. Report No.	2. Government Accession No.	3. Recipient's Catalog No.
NASA CR-187103		

4. Title and Subtitle

ADVANCED ELECTRIC PROPULSION RESEARCH - 1990

5. Report Date
May 1991

6. Performing Organization Code

7. Author(s)

Jeff M. Monheiser
Paul J. Wilbur

8. Performing Organization Report No.

10. Work Unit No.

9. Performing Organization Name and Address

Department of Mechanical Engineering
Colorado State University
Fort Collins, CO 80523

11. Contract or Grant No.
NGR-06-002-112

13. Type of Report and Period Covered
Annual
Jan. 1, 1990-Jan. 1, 1991

12. Sponsoring Agency Name and Address

National Aeronautics and Space Administration
Washington, D.C. 20546

14. Sponsoring Agency Code

15. Supplementary Notes

Grant Monitor - Vincent K. Rawlin, NASA Lewis Research Center
Cleveland, Ohio 44135

16. Abstract

An experimental study of impingement current collection on the accelerator grid of an ion thruster is presented. The equipment, instruments and procedures being used to conduct the study are discussed. The contribution to this current due to charge-exchange ions produced close to the grid is determined using a volume-integration procedure and measured ion beam current density, computed neutral atom density and measured beam plasma potential data. This current, which is expected to be almost equal to that measured directly, is found to be an order of magnitude less. The impingement current determined by integrating the current density of ambient ions in the beam plasma close to the grid is found to agree with the directly measured impingement current. Possible reasons for the disagreement between the directly measured and volume-integrated impingement currents are discussed.

17. Key Words (Suggested by Author(s))	18. Distribution Statement
Electrostatic Ion thruster Impingement Current Charge-Exchange Ions	Unclassified-Unlimited

19. Security Classif. (of this report)	20. Security Classif. (of this page)	21. No of pages	22. Price*
Unclassified-Unlimited	Unclassified-Unlimited	57	

NASA FORM 1626 OCT 86

*For sale by the National Technical Information Service, Springfield, Virginia 22161

Table of Contents

List of Figures

List of Tables

ACCELERATION ELECTRODE ION IMPINGEMENT RESEARCH

Introduction

Positive ions and neutral atoms exit an ion thruster together by passing through its ion acceleration electrodes (grid system). In so doing, the beam ions are accelerated to a high velocity while the neutrals drift through at a much slower, thermal velocity. These two groups of particles usually pass through the grid system without interacting, but occasionally charge-exchange reactions occur. The end result of each reaction is a fast moving neutral, ejected with a speed comparable to that of the fast-moving beam ions, and a slow-moving charge-exchange ion. The charge-exchange ion can, depending on the electric field environment in which it is created, be accelerated into the negatively biased acceleration electrode (the accel grid) or be drawn away from it. Typically, ions accelerated into the accel grid will impinge with a substantial kinetic energy thereby sputter eroding it. The lifetime of a grid system may be determined by the extent to which this unavoidable, ion impingement process can be limited.

A typical pair of grid system apertures through which ions and neutrals pass is sketched in Fig. 1a. A qualitative plot showing the variation of potential along the centerline of these apertures is shown beneath the sketch in Fig. 1b. As Fig. 1 suggests the ions, created upstream of the plasma sheath, are generally assumed to begin the acceleration process where the potential begins to decrease at the sheath. The ions that do not undergo a charge-exchange reaction are accelerated through the region from the screen grid to the accel grid and are then decelerated as they

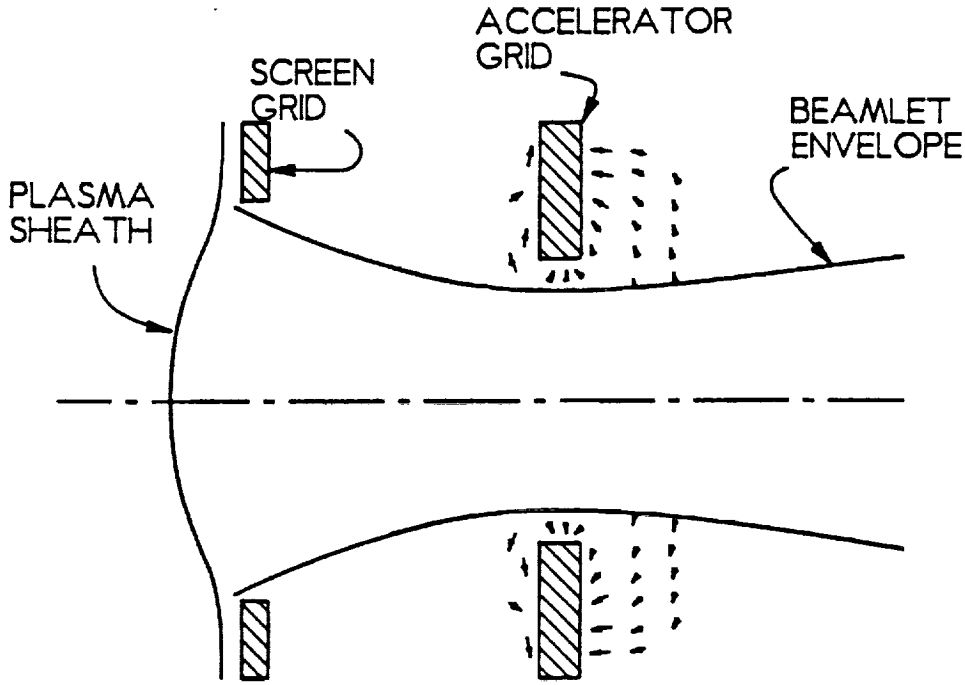

a) Typical Pair of Apertures

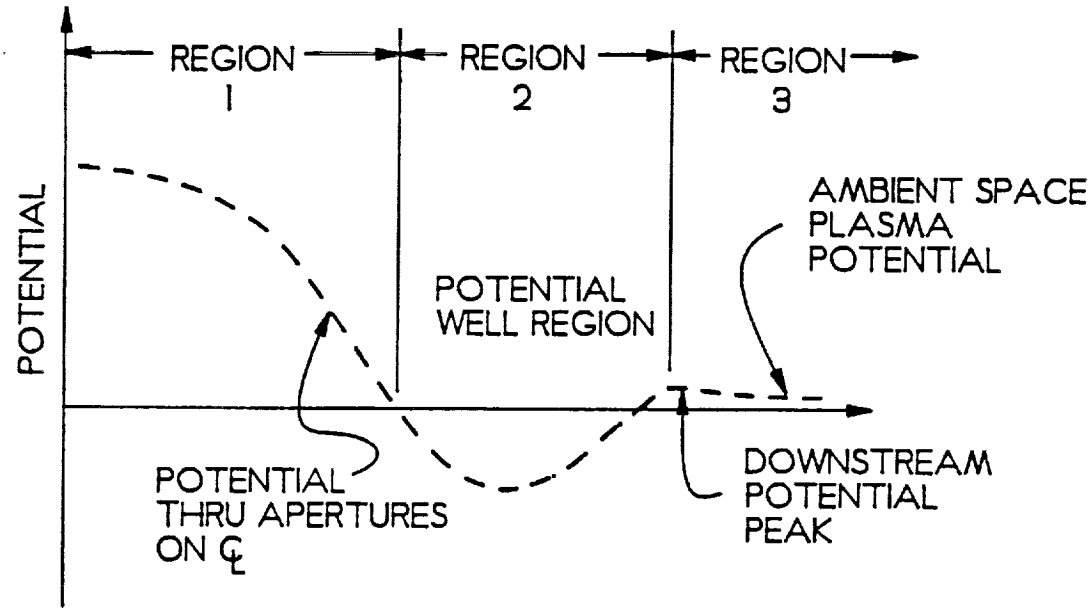

b) Potential Profile Along the Centerline of the Apertures

Fig. 1 Grid System Definitions

exit from the accel grid. They reach a desired, high, final velocity in the ambient space plasma where the potential is uniform and they are generally confined within a beamlet envelope like the one shown in Fig. 1a. Following the convention suggested by Staggs, Gula and Kerslake [1], the beamlet can be divided into the three regions, shown in Fig. 1b, within which the charge-exchange ions behave differently. Those originating in Region 1 (upstream of the potential well) should generally gain enough kinetic energy to escape the grid system, even though they may be on rather divergent trajectories in some cases. Because they escape, these ions would not contribute to the sputtering of the accel grid. The charge-exchange ions created within Region 2 (the potential well) cannot escape into the ambient space plasma, so they will be drawn into the accel grid and sputter erode it. Those created in Region 3 would be expected to flow away from the grids as a result of the force induced by the weak downstream electric field there. Peng, Keefer and Ruyten have suggested that charge-exchange ions will have trajectories like those indicated by the small arrows on Fig. 1a [2].

It should be noted that ions which originate at the plasma sheath can also contribute to sputtering of the accel grid by striking it directly and, due to their higher energies, they will erode it even more rapidly than charge-exchange ions. It is important to distinguish between this direct ion impingement component, which develops when ion beamlets are not properly focused, and the charge-exchange ion impingement component. The former can be reduced to a negligible level through proper design and operation of the grid system. The latter, on the other hand, can

be limited, but not eliminated, because concurrent ion and neutral flow through the grid system is a natural consequence of ion thruster operation. It is also noted that charge-exchange ions that impinge on the accelerator grid are separated into two groups, namely those created between the upstream boundary of the potential well region and accelerator grid (Group A) and those created between the accelerator grid and the downstream potential peak (Group B). In the experiments to be described in this report, the current associated with the Group B ions could be determined but that associated with Group A could not. Fortunately, Peng, et. al. [2] suggest that those in Group B contribute most of the charge-exchange impingement current.

When researchers began to use inert gases (xenon, krypton and argon) rather than mercury in ground-based ion thruster tests, a general increase in the ratio of the impingement-to-beam currents that was typically less than 0.25% to about 1% was observed [3]. For example, a SERT II thruster [4] was modified at Colorado State to utilize high perveance dished grids and a 2.8 mA impingement current was measured when a 730 mA mercury ion beam was being extracted from it (0.4% impingement-to-beam current ratio). Several years later essentially the same thruster operating on xenon at about the same beam current exhibited an 11.5 mA impingement current (1.6%) [5]. While there were several possible reasons why the switch from mercury to inert gases could have induced an increase in the impingement-to-beam current ratio, a general rise in ambient vacuum chamber pressures (and therefore the ambient neutral densities) was considered a

likely cause. In the case of the Colorado State 730 mA beam current tests of the modified SERT II thruster, a 4 μTorr ambient pressure was measured with mercury while 8 μTorr was measured with xenon. The higher ambient pressures developed with xenon because it does not condense as readily on cold surfaces as mercury does and it is therefore more difficult to pump. A comparison of computed charge-exchange-induced impingement currents for both xenon and mercury made using a first-order model [6] suggests, however, that the observed increases in pressure tend to be insufficient to explain the increase in impingement current that is observed with inert gases. Hence further investigation is considered necessary. It is important that the difference between results obtained with mercury and xenon be explained so a reliable model of the impingement current process can be verified and ground-based thruster tests can be used with confidence to predict in-space thruster performance.

The focus of the work described herein has been on the impingement current due to charge-exchange ions produced downstream of the accelerator grids (i.e. Group B ions). The effort is directed at 1) the measurement of this current for an ion thruster operating over a range of conditions, 2) the attainment of an understanding of the physical processes involved and 3) the development of a model based on this understanding that can be used to compute this component of impingement current for various propellants and under various operating conditions. This report describes the current state of progress toward these goals.

Apparatus and Procedure

The key piece of apparatus being used in this study is a SERT II ion thruster [4] that has been modified so it can be operated on xenon propellant at high perveance levels. The specific changes made to the original thruster include the installation of 1) a 0.64 cm diameter main hollow cathode, 2) separate main and hollow cathode propellant feed systems, 3) a movable 0.64 cm diameter hollow cathode neutralizer and 4) a set of high perveance, dished grids. These grids have screen grid hole diameters, d_s, of 1.9 mm; accel grid hole diameters, d_a, of 1.4 mm; a grid separation distance, ℓ_g, of 0.6 mm; a screen grid thickness, t_s, of 0.4 mm and an accel grid thickness, t_a, of 0.5 mm. The main and neutralizer hollow cathodes are made from 6.4 mm diameter tantalum tubes and tungsten orifice plates and they have 1 mm and 0.76 mm diameter orifices, respectively. Both of these cathodes utilize rolled tantalum foil inserts treated with chemical R-500* and torroidal, tantalum keepers with inner and outer diameters of 4 mm and 2 mm, respectively.

As shown in Fig. 2, the neutralizer hollow cathode is supported by the tube through which xenon expellant is supplied to it. This tube can be rotated to move the neutralizer discharge from radial locations near the thruster centerline to ones as much as 30 cm from the centerline. The neutralizer can also be moved axially from the plane tangent to the accel grid at its centerline to a plane 50 cm

---

* R-500 is a double carbonate ($BaCO_3$, $SrCO_3$) mixture that has been manufactured by the J.R. Baker Chemical Co., Phillipsburg, N.J. but is no longer made.

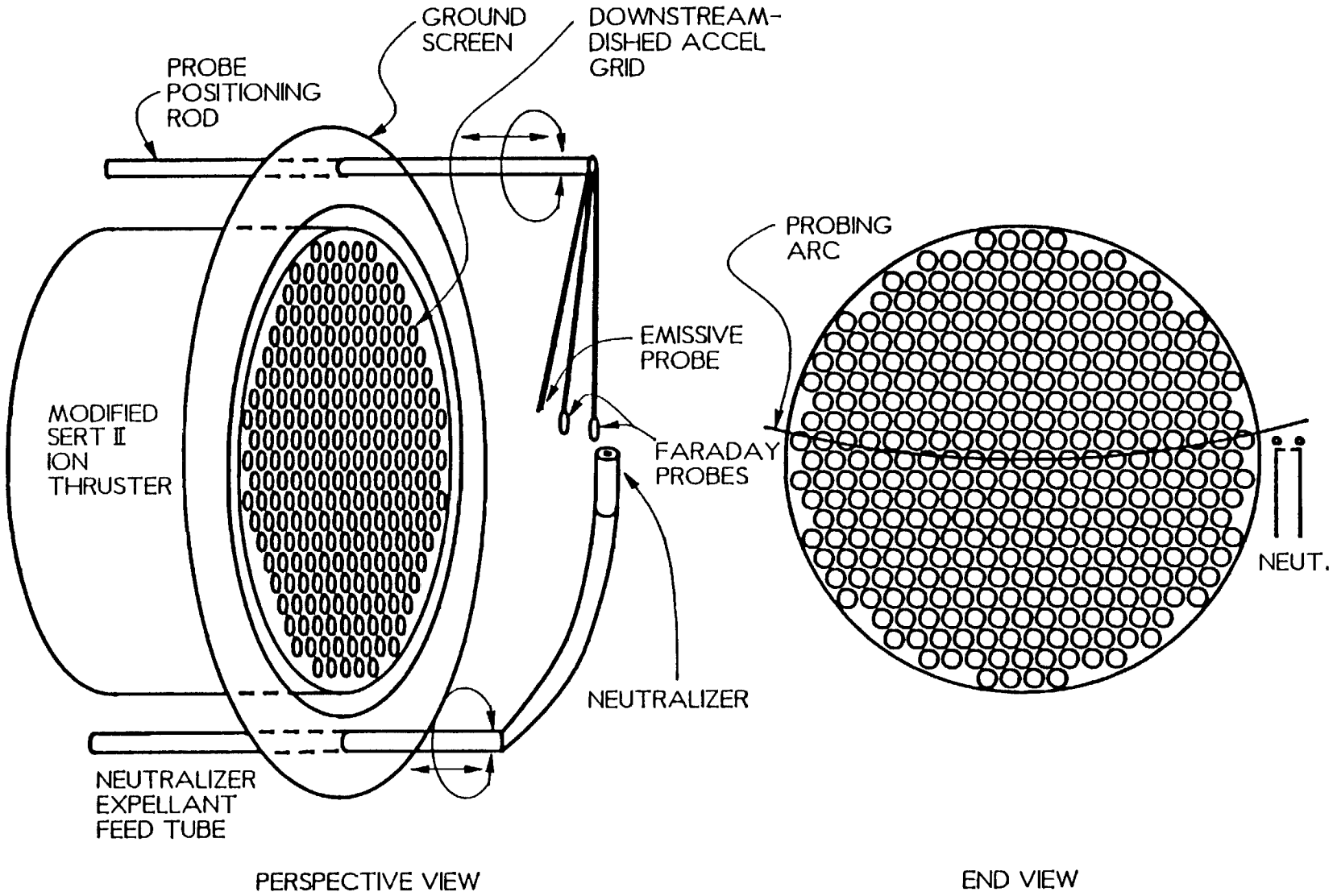

Fig. 2 Mechanical Schematic of Neutralizer and Probes

downstream of the grid. Thus, the effects of neutralizer position on the production of Group B charge-exchange ions can be studied. Although the neutralizer shown schematically in Fig. 2 was used for most of the tests described here, one test was conducted in which a separate plasma source located 2.7 m from the thruster on the tank centerline was used to demonstrate the effect of a neutralizer located far from the thruster grids.

The physical arrangement of the probes used to measure conditions in the ion beam plasma downstream of the thruster are also shown in Fig. 2. These probes can also be moved axially and they are mounted together in such a way that they are each swept on an arc that passes through the thruster centerline at each axial location. When the probes and neutralizer are at the same axial location, this arc passes within a few millimeters of the neutralizer keeper position as shown in the end view of Fig. 2. The probe assembly contains an emissive probe and two Faraday probes and by moving them axially and radially, measurements can be made with each probe throughout the region extending from near the thruster grids to a plane 17 cm downstream of them and to radial locations 11 cm on either side of the thruster centerline. One of these Faraday probes is sighted upstream (i.e. towards the grids) and is used to measure ion beam current density profiles and is hence designated the beam ion probe. Its sensor can be swept on arcs from 0.2 to 17 cm downstream of the plane tangent to the dished accel grid at the thruster centerline. A second Faraday probe with its sensor sighted downstream (i.e. away from the accel grid) can be swept on an arc at axial positions ranging from 0.6 to

17 cm downstream of the accel grid at the thruster centerline. This probe is designated the ambient ion probe and it is used to measure ion current density profiles associated with ions flowing upstream toward the accel grid. An ambient ion current density profile, obtained close to the accel grid, is probably the most important of these data because it may be representative of the impingement current due to Group B ions. Finally, a floating emissive probe, which is used to sense potential profiles in the beam plasma, can be swept on arcs ranging from axial positions of 0.2 to 17 cm downstream of the accel grid tangent plane. The sensor for this probe, a 0.08 mm diameter tungsten wire formed into a 3 mm diameter loop, yields beam plasma potentials with a good resolution on the scale of the beam diameter, but not on the scale on individual beamlets extracted by the high perveance grid set being used. The ground screen, shown in Fig. 2, serves to prevent beam plasma electrons from reaching the thruster body. It was designed to lie close to the accel grid so it would not interfere with the probes as they were swept radially through planes close to the grid.

The beam ion and ambient ion Faraday probes used in this study were identical, and the key physical features of the design are illustrated in Fig. 3. They include a thin profile that facilitates sensor (collector) positioning as close to the accel grid as possible when the probe is facing downstream. The stainless steel probe body is 4 mm thick and it is attached to a 3.2 mm diameter grounded, copper support tube. Copper is used to provide a high conductance path for the removal of the heat deposited by the beam. This heat removal capability prevents the

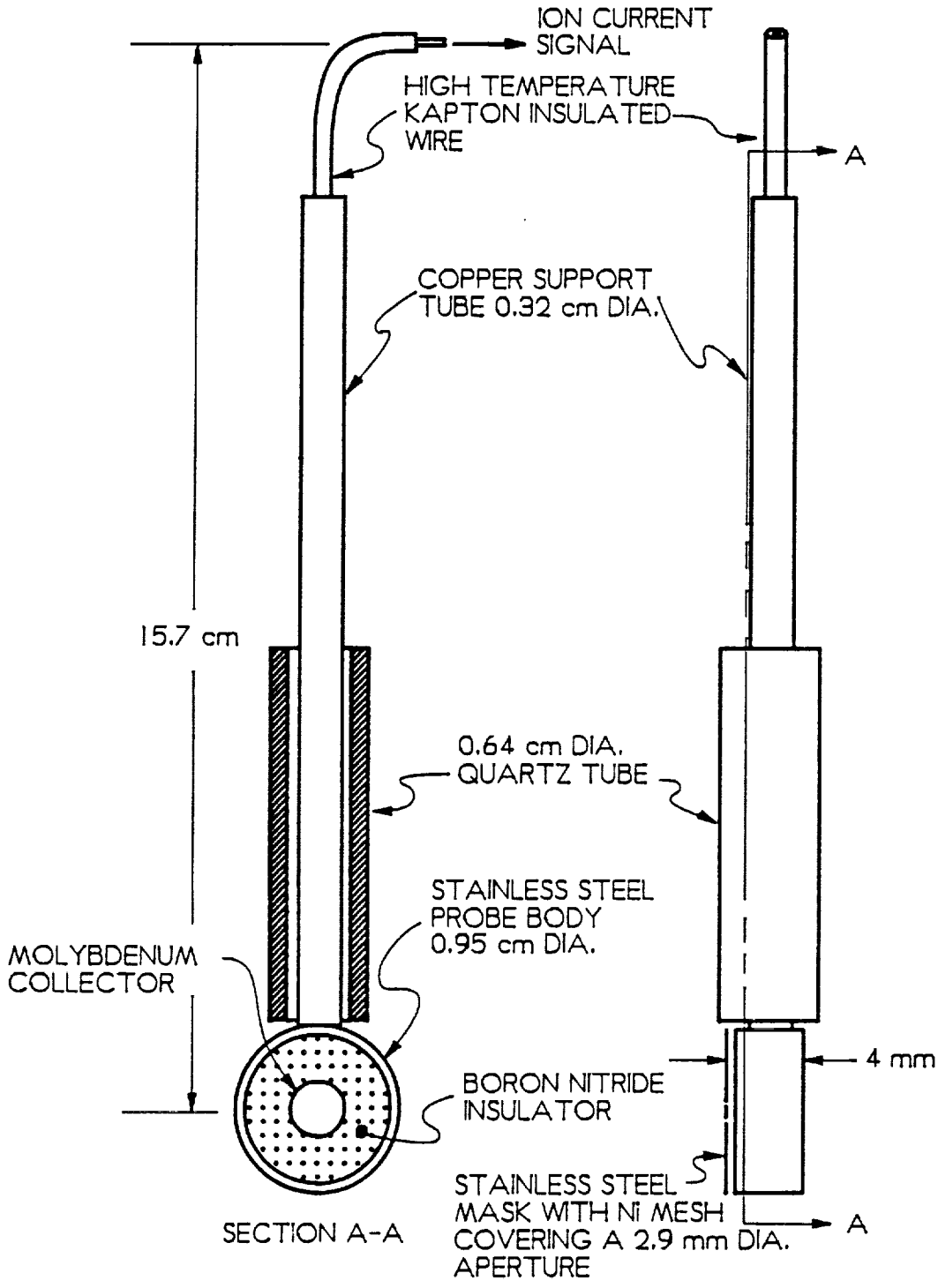

Fig. 3 Mechanical Schematic of the Beam and Ambient Ion Faraday Probes

significant temperature rises along the tube and at the sensor, that can lead to a loss of the electrical isolation needed to assure accurate measurement of the small collector currents drawn into the probes. The 6.4 mm o.d. quartz tube that surrounds the copper tube serves to prevent sputtering of the copper by beam ions. The ion collector is made of molybdenum so errors caused by secondary electron emission induced by beam ions will be minimized. In order to assure planar electric fields at the collector, an 80% open area fraction nickel mesh with square openings 0.24 mm on a side, was stretched over a 2.9 mm diameter aperture in the stainless steel mask shown in Fig. 3. Each collector was held at a potential below that of the neutralizer cathode so that energetic electrons from the neutralizer cathode, that are present in the beam plasma, would be repelled and would not therefore introduce an error in the ion current signal being measured. Frequently, this requirement meant that the collector was held $\sim$20 V below ground.

An electrical schematic that shows the power supplies, the volt meters, and the ammeters required to sustain and characterize the operation of the thruster is given in Fig. 4. Included on this figure are meters that measure the screen voltage, V_+; the accel voltage, V_-; the beam current, J_B; the impingement current (measured directly) J_{id}; the keeper voltage, V_K; the keeper current, J_K; the discharge voltage, V_D and the discharge current, J_D. Also shown in Fig. 4 are the supplies used to power the neutralizer hollow cathode discharge and the instruments used to measure the neutralizer keeper voltage and current, V_N and J_N; the coupling voltage, V_C and the neutralizer emission current, J_E.

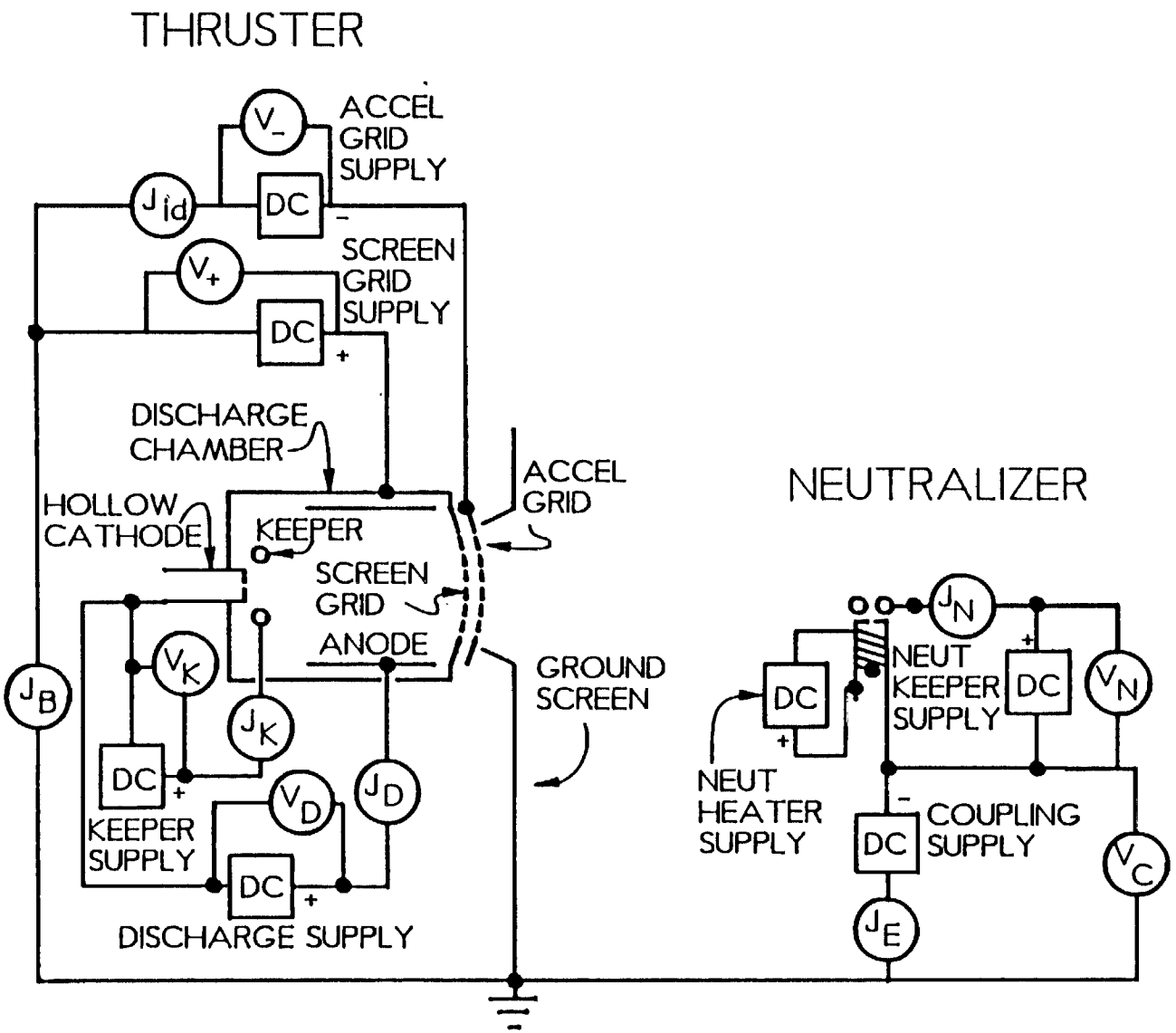

Fig. 4 Electrical Schematic

All experiments were conducted in a 1.2 m diameter by 5 m long vacuum chamber using xenon as the propellant. They were typically carried out by first starting the ion thruster and neutralizer hollow cathodes and stabilizing their operation at the desired propellant flow condition and keeper currents of 300 mA. Next, the anode was biased positive, a discharge was established and the screen and accel voltages were raised to their operating values (V_+ = 1000 V and V_- = -500 V). Thruster operation was stabilized by controlling the discharge current to maintain the desired beam current and biasing the neutralizer to realize a neutralizer emission current that matched the beam current, i.e. $J_E = J_B$. All of the pressure readings given in this report were measured using a cold cathode gauge; the measured readings were all corrected to reflect the gauge calibration factor for xenon. They are considered correct to within the typical accuracy of cold cathode gauges ($\pm$ 100%).

Once thruster operation was stable, Faraday and emissive probe data were collected in the beam using a computerized data acquisition system. This system uses an XT compatible computer with an HP-IB interface card to communicate with a Tektronix 7854 digitizing, dual-channel oscilloscope. The beam potential data are collected with the system by positioning the floating emissive probe at a given axial position and recording the potential at which it floats as a function of radial position. At each axial position, 512 beam plasma potential data points are recorded on one channel and 512 points, corresponding probe radial position, which was measured as a voltage across potentiometer, are recorded on the second

channel. Both signals are recorded simultaneously as a function of time and the time variable is eliminated later to obtain beam plasma potential vs. radial position data. This data collection process is repeated at as many axial positions as desired to yield the desired detail and extent of the beam plasma potential field throughout the region downstream of the thruster.

The ion current collected by the beam ion Faraday probe is measured as a function of radial position at any desired axial position using the same procedure just described for the beam plasma potential data. Beam ion current density data are obtained from measured ion current data by dividing each ion current data point by the sensing area of the Faraday probe. Similarly, the ambient ion Faraday probe can be used to measure the ion current density of low energy ions in the ambient beam plasma as a function of radial position at any desired axial position.

The accuracy of beam ion Faraday probe data can be checked by integrating the beam ion current density data over the beam area and comparing it to the measured beam current, J_B. In the present experiments, beam currents determined using these two independent methods generally agreed within 15%.

Interpretation and Comparison of Impingement Current Data

The data being collected is these experiments can be used to determine accel grid impingement current in three independent ways. First, it can be measured directly as the electron current, J_{id}, that must be supplied to the accel

gird to neutralize ions that impinge on it (Fig. 2). Second, it can be determined by measuring the "upstream flowing" ambient ion current density profile using the ambient ion Faraday probe positioned near the accel grid. This profile is then integrated over the accel grid area to obtain the area-integrated impingement current, J_{iA}. A third impingement current, $J_{i\forall}$, can be found by integrating the rate of charge-exchange ion production over the volume from which charge-exchange ions are drawn into the accel grid. This volume is defined as the one in which the gross potential gradients are such that charge-exchange ions would be expected to be accelerated towards and impinge upon the accel grid. The first two of these impingement currents are determined through straightforward measurement and analysis, but the latter one is more complex and requires some explanation. The rate at which charge-exchange ions are produced in a volume $\forall$ is given by

$$J_{i\forall} = \int_{\forall} e\, n_n\, n_i\, v\, \sigma_{ce}\, d\forall \quad , \tag{1}$$

where e is the electron charge, n_n is the neutral density, n_i is the beam ion density, v is the beam ion velocity, σ_{ce} is the charge exchange cross section and $\forall$ is the charge-exchange ion extraction volume. Noting that the product "$v\, n_i\, e$" is the beam current density, Eq. 1 can be rewritten

$$J_{i\forall} = \int_{\forall} n_n\, j_B\, \sigma_{ce}\, d\forall = \int_{\forall} R_{ce}\, d\forall \quad , \tag{2}$$

where R_{ce} is the charge-exchange reaction rate per unit volume. This integral can

be evaluated as the product of the xenon charge exchange cross section (pertaining to the beam ion energy), the beam ion current density and neutral xenon density determined as a function of radial/axial position. This product is then integrated over the charge-exchange ion extraction volume $\forall$, yielding the volume-integrated impingement current, $J_{i\forall}$. The needed cross section is available in the literature [7], the beam current densities will be measured and the neutral densities will be calculated. In general, the neutral density and beam current density will be strong functions of radial position immediately downstream of the grids because ion and neutral beamlets issue from each individual accel grid hole. The integration indicated in Fig. 2 will as a result be difficult to carry out. In order to avoid this difficulty, the approach used here will be to use mean beam ion current densities and neutral densities (i.e those that do not reflect the detailed beamlet structures) and a gross charge-exchange ion volume to evaluate Eq. 2.

In order to determine the appropriate gross charge-exchange ion extraction volume for application in Eq. 2, it is generally assumed that charge-exchange ions will be produced with negligible kinetic energy. In this case, the volume is the one where beam plasma potential gradients are such that a newly produced charge-exchange ion will be directed at the accel grid. These potential gradients can be numerically determined from measured beam plasma potential data presented in topological plot format like that for the hypothetical beam plasma potential data shown in Fig. 5. The cross-hatched region in the plot represents a first order estimate of the volume of interest. Downstream of this region, axial

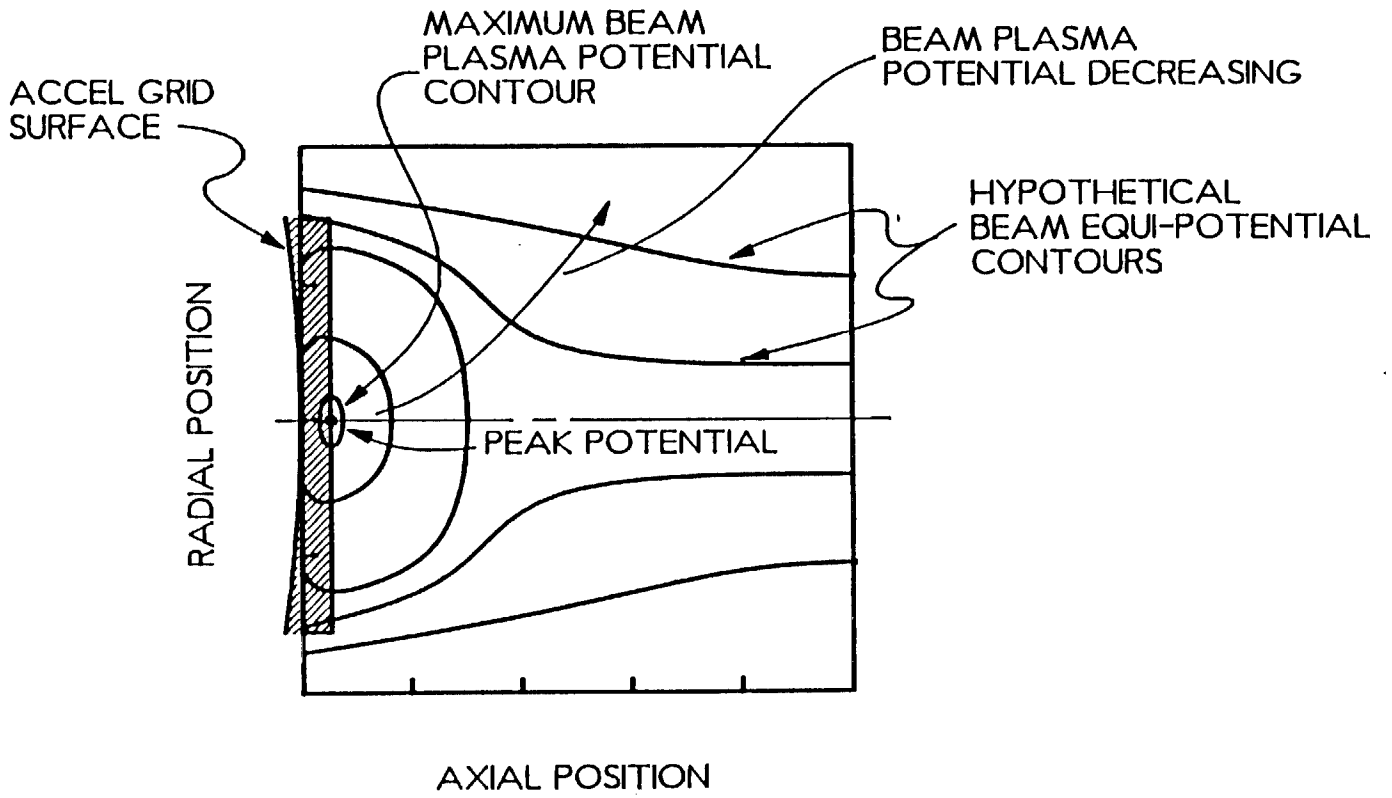

Fig. 5 Hypothetical Beam Plasma Potential Contour Plot Showing the Charge-Exchange Ion Extraction Volume

components of the beam plasma potential gradients are such that newly produced charge-exchange ions would feel a component of force directed downstream. Within the region, the opposite would be true, and the axial force component felt by newly formed ions would be directed toward the accel grid. In this hypothetical case, the downstream boundary of the charge-exchange ion extraction volume is a plane perpendicular to the centerline, the radial boundary is cylindrical with a radius equal to the beam radius and the upstream boundary is the accel grid surface. When beam plasma potential maps are generated from experimental data, they are not as well behaved as suggested by Fig. 5 and the downstream boundary will typically not be planar. For this preliminary work, however, it was assumed that it was planar and perpendicular to the centerline and that it passed through a beam plasma potential peak that could generally be identified readily. This procedure yields gross charge-exchange ion extraction volumes that are considered to be about 20% greater than values that would be obtained if the curvature of the downstream boundary were considered.

A more accurate value for the gross charge-exchange ion extraction volume could be determined numerically, from a plot of measured beam plasma potential data, by computing the trajectories of zero-velocity ions from many points throughout the beam plasma region near the grids. The volume of interest would then be the one within which the ions would be drawn to the accel grid. The accuracy of this volume would be determined by the resolution of probe used to measure the beam potential data. For this preliminary study, however, where first

order comparisons of impingement currents are being made, gross charge-exchange ion extraction volumes like the one shaped as shown by the cross-hatched area in Fig. 5 will be used to compute the volume-integrated impingement currents.

Estimates of the gross charge-exchange ion extraction volume are made from experimental beam plasma potential data in the following way. First, the experimental beam plasma potential points, needed to draw potential maps, are interpolated using an inverse-distance-squared procedure [8] to obtain values for beam plasma potential data at evenly spaced grid points. This procedure is accomplished using the program "SURFER", and for the data included in this report the grid size was held constant at 0.25 cm in both the radial and axial directions. Next, these data are plotted in topological and 3-D surface formats again using "SURFER". Finally, the axial distance to the downstream potential peak is determined from the topological plot and the gross estimate for the volume is computed using this distance.

The neutral density throughout the region downstream of the accel grid, needed as input to Eq. 2, is computed rather than measured. This is accomplish using a free-molecular flow model developed to predict the density distribution downstream of a multi-hole, thin, planar plate through which neutrals flow at a prescribed rate into a region that is at a prescribed ambient density far downstream of the plate. The details of this model are described in Appendix A to this report. Using the computed downstream neutral density distribution together with the measured ion beam current density, charge-exchange cross section and the gross

estimate for the charge-exchange ion extraction volume, Eq. 2 can be applied to compute the volume-integrated impingement current, J_{iV}. This result can then be compared to the impingement current measured directly, J_{id}, and the value obtained by integrating the ambient ion current density adjacent to the accel grid, J_{iA}.

Results

Comparisons between accel grid impingement currents obtained by 1) direct measurement, J_{id}; 2) integrating the ambient ion current density (adjacent to the accel grid) over the area of the accel grid, J_{iA}, and 3) integrating the model of charge exchange ion production over the charge-exchange ion extraction volume, J_{iV}, were performed using data obtained from the modified SERT II ion thruster operating at the conditions listed in the left-hand column of Table 1. Many of the symbols used to define the operating conditions in the table are identified in Fig. 4. Those which were not are the main propellant flow rate, $\dot{m}_m$, the propellant flow rate through the hollow cathode, $\dot{m}_c$, and through the neutralizer hollow cathode flow rate, $\dot{m}_N$; the vacuum tank ambient pressure, P_o, and the discharge chamber propellant utilization efficiency, η_u. The final symbols (r_N and z_N) define the radial and axial coordinates of the neutralizer measured relative to the thruster centerline and its intersection with the accel grid. Also shown for comparative purposes are similar operating conditions associated with a test conducted several years ago with essentially the same thruster operating on mercury.

Table 1 indicates that the directly measured impingement current was

Table 1

Modified SERT II Thruster Operating Conditions

Present Test (Xenon)	Previous Test (Mercury)
$V_+ = 1000$ V	1000 V
$V_- = -500$ V	-500 V
$V_D = 45$ V	32 V
$J_D = 2.4$ A	1.8 A
$V_K = 11$ V	8 V
$J_K = 300$ mA	300 mA
$V_N = 19$ V	19 V
$J_N = 300$ mA	200 mA
$\dot{m}_m = 180$ mA eq. (Xe)	270 mA eq. (Hg)
$\dot{m}_c = 90$ mA eq. (Xe)	160 mA eq. (Hg)
$\dot{m}_N = 90$ mA eq. (Xe)	-----
$P_o = 3 \times 10^{-6}$ Torr	3×10^{-6} Torr
$V_C = -20$ V	-16 V
$J_B = J_E = 230$ mA	312 mA
$J_{id} = 2.1$ mA	1.6 mA
$\eta_u = 84\%$	73%
$r_N = -10$ cm	-5 cm
$z_N = 1$ cm	5 cm

2.1 mA at the operating condition for the present test. Figure 6a shows the 3-D surface plot of the ambient ion current density measured as a function of radius and axial position using the ambient ion Faraday probe. Experimental data were measured at axial locations beginning 0.6 cm downstream of the accel grid because this was the closest to the grid that the probe could be positioned. The data shown between this axial position and the accel grid (zero) were determined by extrapolation. Figure 6b shows the axial variation in the area-integrated ambient ion current obtained by integrating measured ambient ion current density profiles over 1) the total measurement range, the circle symbols, (i.e. $\pm$ 10 cm radii) and 2) the accel grid area, the square symbols, (i.e. $\pm$ 7.5 cm radii). These data are striking for the following reasons:

1. The area-integrated impingement current (J_{iA} = 2.2 mA in Fig. 6b) determined by integrating the ambient ion current density over the beam area at an axial position of 0.6 cm from the accel grid is very close to the directly measured impingement current (J_{id} = 2.1 mA).

2. There is the evidence of a sharp peak in the ambient ion current density near the neutralizer (r_N = -10 cm, z = 1 cm in Fig. 6a) that one would expect on the basis of accel grid erosion that has been observed when a neutralizer is located close to the accel grid [9].

The fact that the values of J_{id} and J_{iA} agree so well suggests the ambient ion Faraday probe is indeed measuring the current density of charge-exchange ions moving toward the accel grid accurately. This accuracy is surprising when one

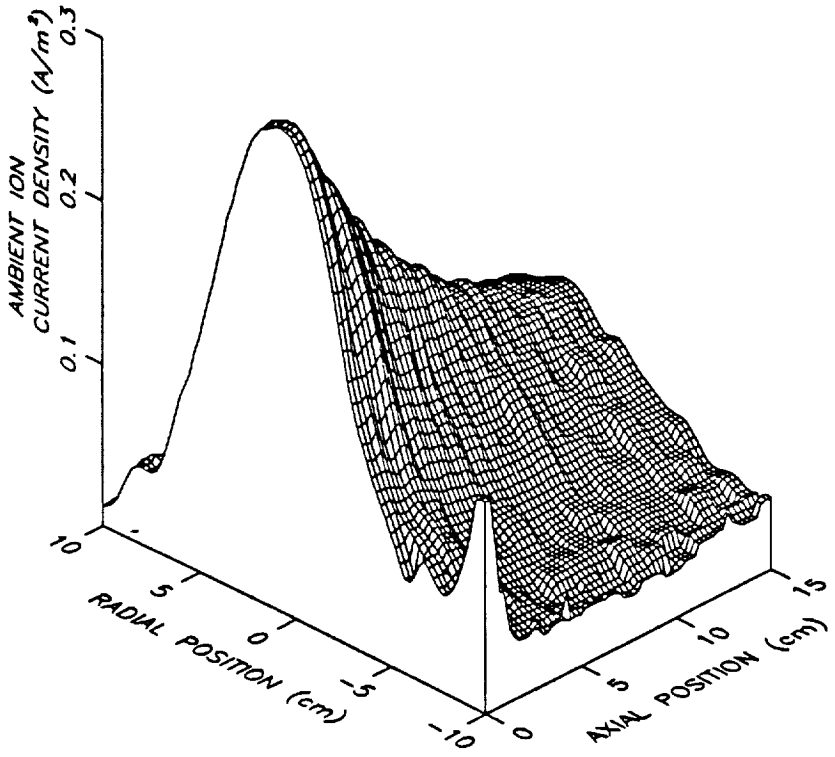

a) 3-D Surface Plot

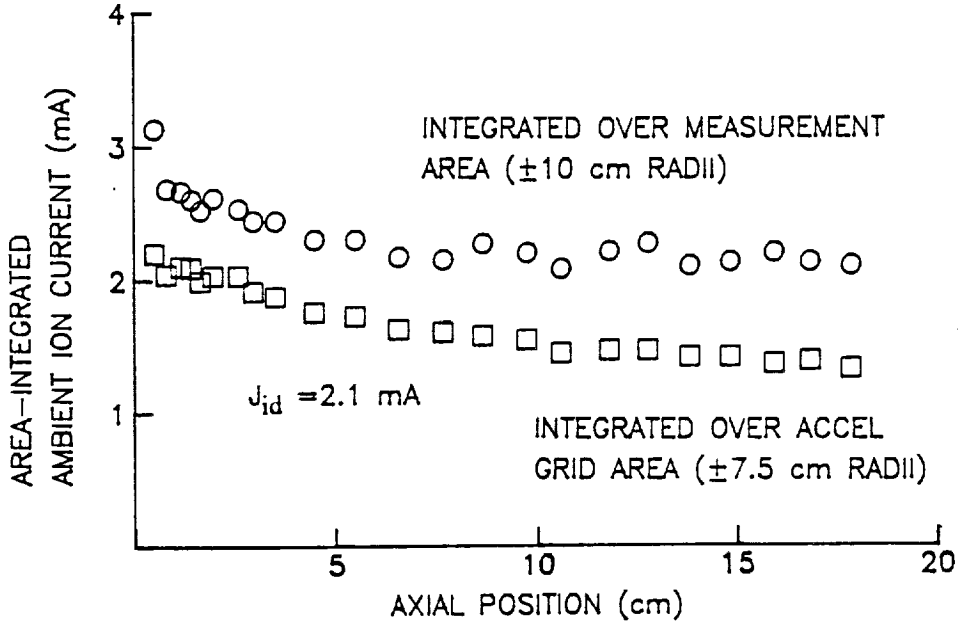

b) Variation of the Area-Integrated Impingement Current with Axial Position

Fig. 6 Ambient Ion Current Density Data for the Operating Conditions of Table 1

considers the fact that the probe itself is interrupting the beam ions and the sensor is, therefore, collecting ambient ions in the probe wake. More work is considered necessary to apply wake theory [10] to the ambient ion current density data so it can be assured that they are being interpreted properly.

Beam ion current density data measured using the beam ion Faraday probe when the thruster was operating at the conditions of Table 1 are shown in Fig. 7. Figures 7a and 7b are, respectively, the 3-D surface and topological plots of the beam ion current density measured downstream of the accel grid. The divergence of the ion beam is reflected in the observation that the current density decays on the centerline and increases at the outer radii. Note that the beam ion current density data shown in Fig. 7a and 7b are identical and that the profile at zero (the accel grid location) in these figures is determined by extrapolation from the profile measured 0.3 cm downstream of this grid and shown in Fig. 7c. Note, however, that Fig. 7c shows the profile seen by an observer looking upstream while those in Figs. 7a and b are presented as seen looking downstream. In the case of these particular data, the measured beam current, J_B, is seen to be $\sim 15\%$ greater than the beam current obtain by integrating the beam ion current density profile at the accel grid $J_{B,int}$. In general, the measured beam was found to be the greater of the two. The reason for this is uncertain, but it could be due to the fact that the mesh covering the probe aperture has a transparency to beam ions that is less than the physical transparency of the mesh.

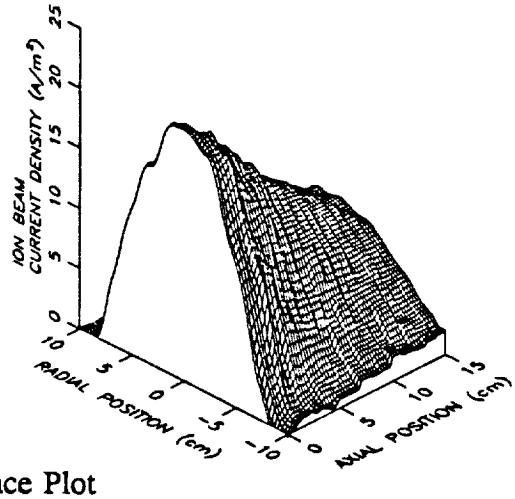

a) 3-D Surface Plot

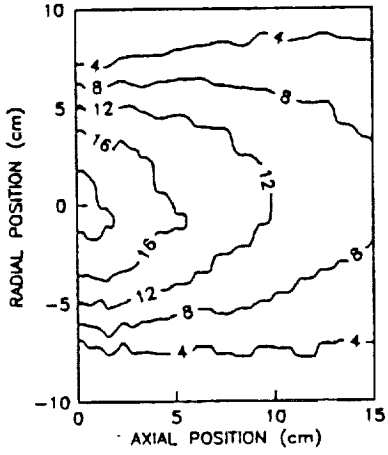

b) Topological Plot (A/m^2)

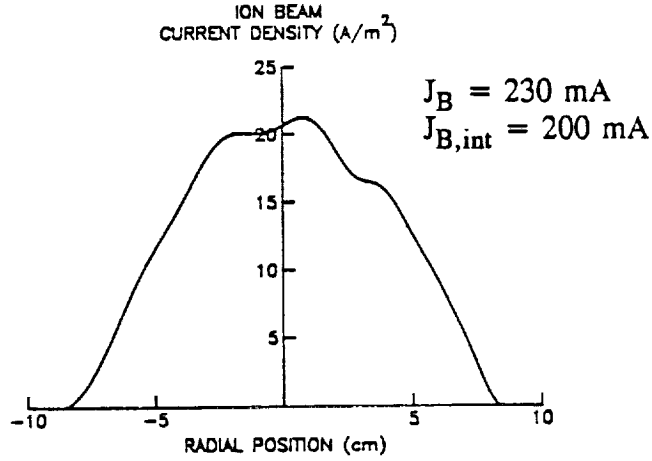

c) Radial Profile near Accel Grid

Fig. 7 Ion Beam Current Density Data at Table 1 Operating Conditions

Neutral density maps computed using the approach of Appendix A at the operating conditions of Table 1 are shown in Fig. 8. As the legend for this figure suggests, a discharge chamber wall temperature (T_w) of 500 K and a vacuum tank temperature (T_o) of 300 K were assumed to obtain these results. It should be noted that the model of Appendix A becomes accurate a few hole diameters downstream of the accel grid. Hence, the data of Fig. 8 in the region between there and the accel grid itself were determined by imposing a linear variation in density from that at the aperture (determined using the sharp-edged orifice free molecular flow model [11]) to those obtained using the methods of Appendix A further downstream.

Combining the data presented in Figs. 7 and 8 with the charge-exchange cross-section for 1000 eV xenon ions (39×10^{-16} cm^2 [7]) into Eq. 2, the charge-exchange ion production rate per unit volume (R_{ce}) can be calculated as a function of radial and axial positions downstream of the accel grid. For the case of operation at the conditions of Table 1, the results of doing this are shown in Fig. 9. This figure shows that the charge-exchange ion production rate is greatest near the center of the accel grid and that it decays to near zero at the edge of the ion beam. This result is consistent with experimental erosion patterns on accel grids that show that charge-exchange ion erosion pits develop most rapidly near the center of the accel grid [12].

The final step in the process of computing the impingement current by integration of the charge-exchange ion production rate over the charge-exchange

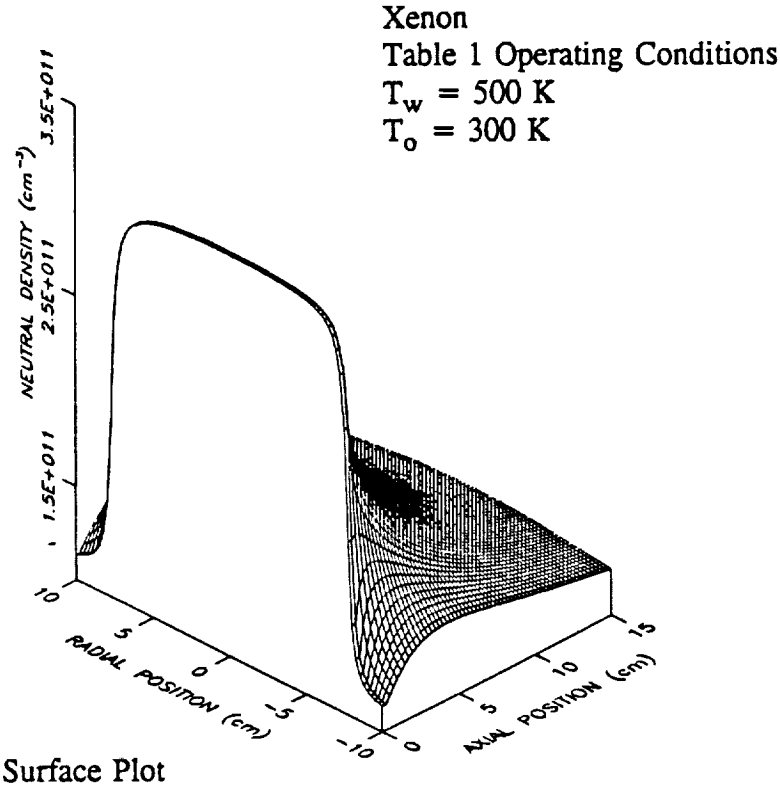

a) 3-D Surface Plot

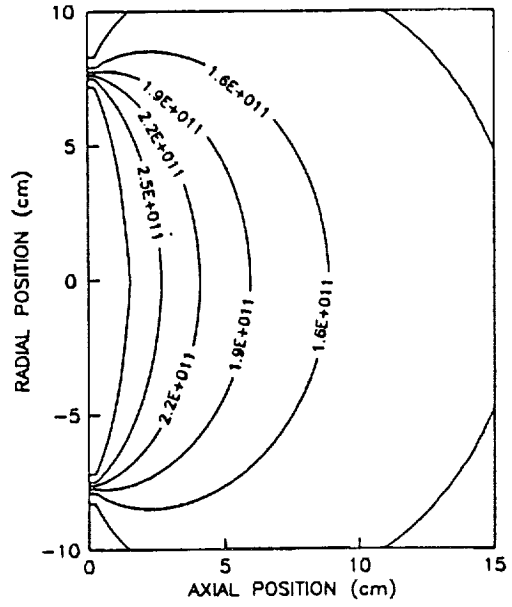

b) Topological Plot (cm^{-3})

Fig. 8 Computed Neutral Density Data

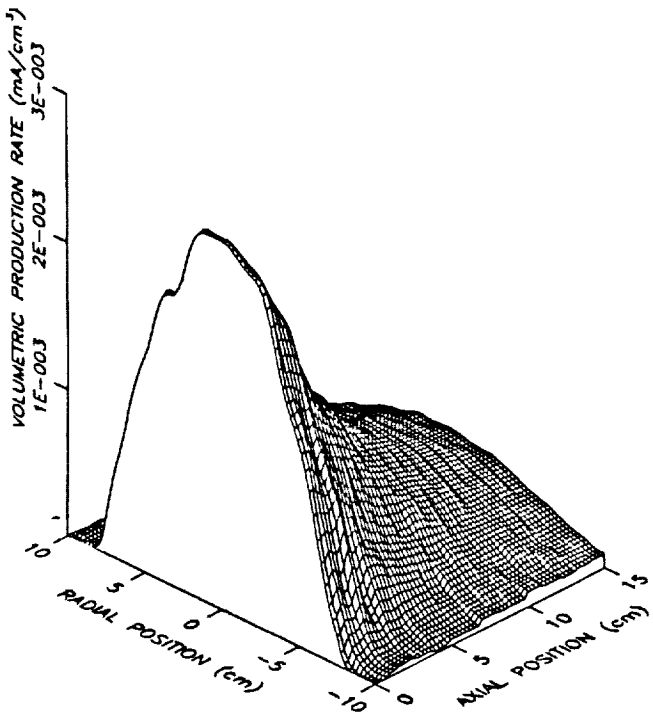

a) 3-D Surface Plot

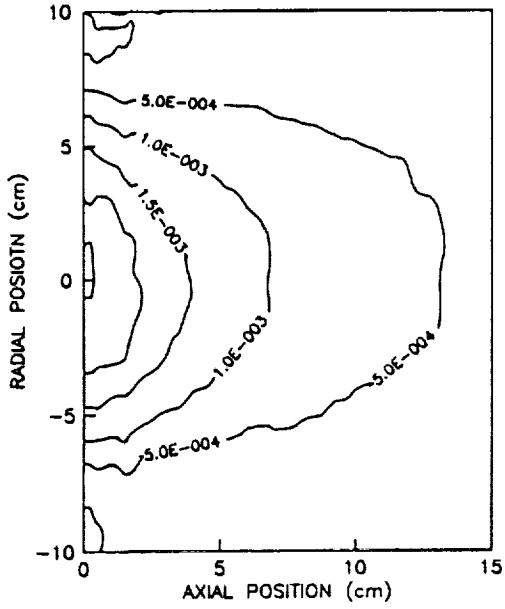

b) Topological Plot (mA/cm^3)

Fig. 9 Typical Charge-Exchange Ion Production Rate Data

ion extraction volume, $\forall$, is to obtain an estimate of this volume. The beam plasma potential data obtained using the floating emissive probe at the conditions of Table 1, which are needed to make this estimate, are presented in 3-D surface map and topological plot formats in Figs. 10a and b. They show a general trend for potentials to decrease with axial downstream position from a maximum quite close to the accel grid. They also show a dramatic drop in potential near the neutralizer (located at an axial position of ~ 1 cm and a radial position of -10 cm). The beam plasma potential profile measured adjacent to the accel grid is shown in Fig. 10c. Note again that the profiles at $z = 0$ in Figs. 10a and b are those that would be seen by an observer positioned downstream, looking towards the ion thruster.

Figures 10a and b indicate that the potential gradients within about ~ 0.5 cm of the accel grid would direct charge-exchange ions towards the accel grid. This value is consistent with the ion "deceleration length" of 0.6 cm computed using the operating conditions of Table 1 and Kerslake's Model [6]. Using the data presented in Fig. 10b to determine the charge-exchange ion extraction volume and evaluating Eq. 2, a volume-integrated impingement current, $J_{i\forall}$, of 0.17 mA was obtained. This estimate of the impingement current is an order of magnitude less than the impingement currents determined by direct measurement ($J_{id} = 2.2$ mA) and by area integration of the ambient ion current density ($J_{iA} = 2.1$ mA) as indicated on Fig. 10. The reason for this difference is not apparent, but it is important that it be found so test results obtained in ground

J_{id} = 2.1 mA
J_{iA} = 2.2 mA
J_{iV} = 0.17 mA

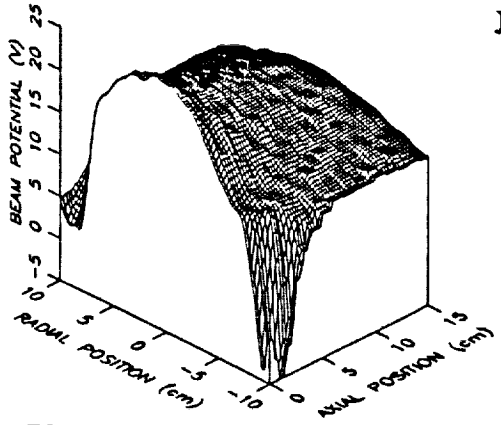

a) 3-D Surface Plot

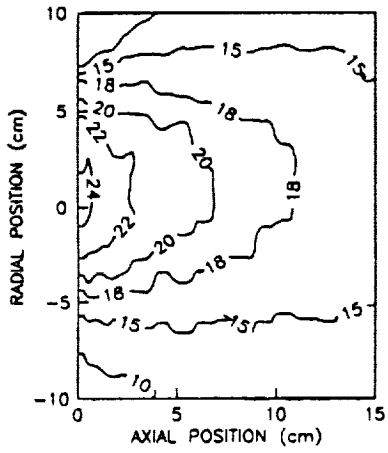

b) Topological Plot (V)

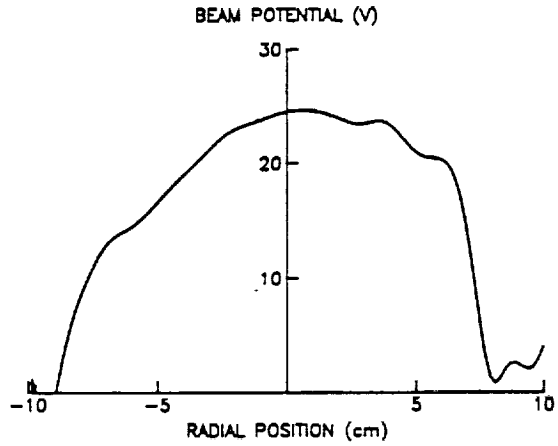

c) Profile Adjacent to Accel Grid (z = 3 mm)

Fig. 10 Typical Beam Potential Data

tests can be interpreted and extrapolated meaningfully to the space operational environment.

In order to evaluate the consistency of the impingement current determined by the volume integration, a second experiment was conducted at the conditions given in Table 1 a day after the data presented in Figs. 6 through 10 were collected. The topological maps of beam plasma potential and the directly measured and volume-integrated impingement currents associated with this two tests are compared in Fig. 11. A comparison of these data shows that the beam plasma potentials were slightly different and this changed the values for the charge-exchange extraction volumes. Still, the data were in relatively good agreement from one day to the next, so the measured and volume-integrated impingement currents differed by more than an order of magnitude on both days. This result suggests that the discrepancy between the directly measured and volume-integrated impingement currents is not anomalous.

In an attempt to determine if neutralizer operation had a dominant influence on the impingement process, the hollow cathode neutralizer discharge was turned completely off and the changes induced in the various profiles and impingement currents were determined. In this test, the thruster operating conditions were held at the values given in Table 1, but the neutralizer keeper current and flow rate were reduced to zero. Under this condition, ion beam neutralization was accomplished via secondary electron emission from vacuum chamber walls and other ground-potential surfaces within the vacuum chamber. The topological beam

Table 1 Operating Conditions
Integration Regions are Shaded

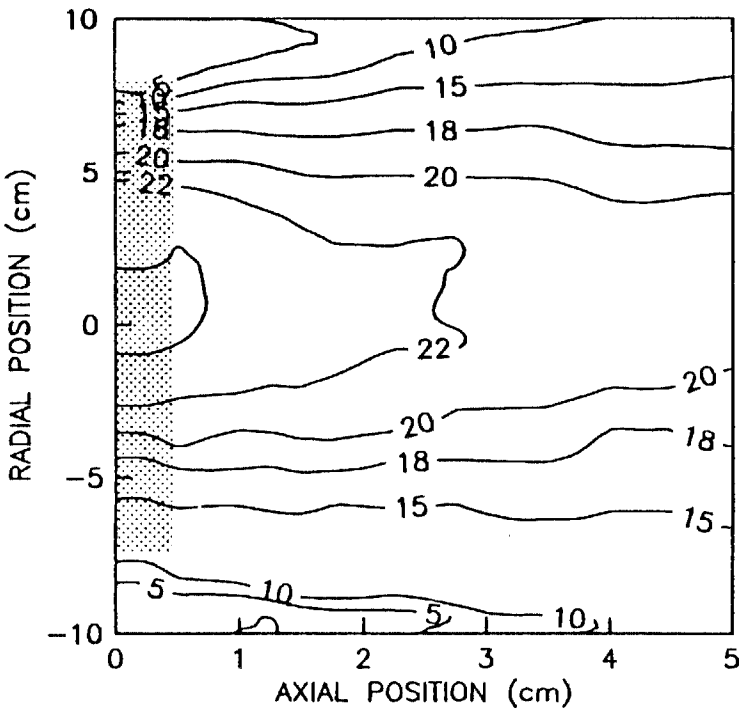

J_{id} = 2.1 mA
J_{iv} = 0.17 mA

a) Beam Plasma Potentials (V)
1st Experiment

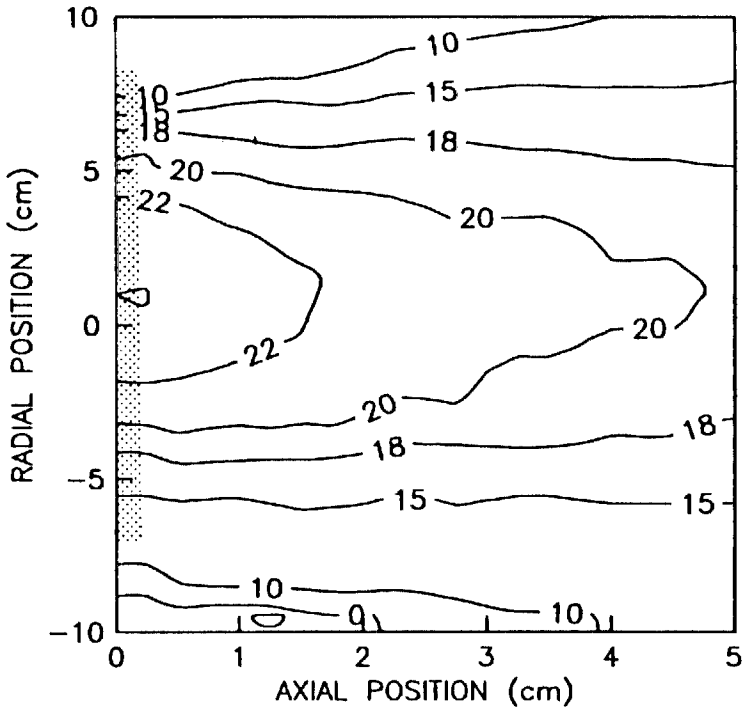

J_{id} = 2.1 mA
J_{iv} = 0.13 mA

b) Beam Plasma Potential Map (V)
2nd Experiment (Next Day)

Fig. 11 Repeatability of Beam Plasma Potential Data and of Volume-Integrated Impingement Currents

plasma potential maps and impingement currents determined in the three ways for the thruster operating without a neutralizer are compared to those associated with the standard data (Fig. 11a) in Fig. 12. A comparison of the beam plasma potential maps in Fig. 12 shows that extinguishing the neutralizer discharge induces an increase in beam plasma potentials and causes the point of maximum potential to move downstream to an axial position of ~ 0.75 cm. This causes the volume-integrated impingement current, J_{iv}, to increase somewhat to 0.30 mA, but it is still about an order of magnitude less than the directly measured impingement current, J_{id}, which remains unchanged. It is also noteworthy that the area-integrated impingement current increased unexpectedly when the neutralizer discharge was turned off. All of these results suggest inconsistencies that must be resolved.

The effect of neutralizer position on the impingement currents was investigated by moving the neutralizer from its original axial position of ~ 1 cm downstream of the accel grid to an axial position 17 cm downstream of it. The movable neutralizer was then turned off and a second neutralizer located 270 cm downstream of the grids was turned on. Values of the impingement currents were determined using the three different methods for neutralizer axial positions of 1, 17, and 270 cm downstream of the accel grid. The results, which are presented in Fig. 13, show again that the directly measured and area-integrated impingement currents agree well, but the volume-integrated value, which has been multiplied by ten in the figure, is still an order of magnitude low. Further, the figure shows no

Table 1 Operating Conditions
Integration Regions are Shaded

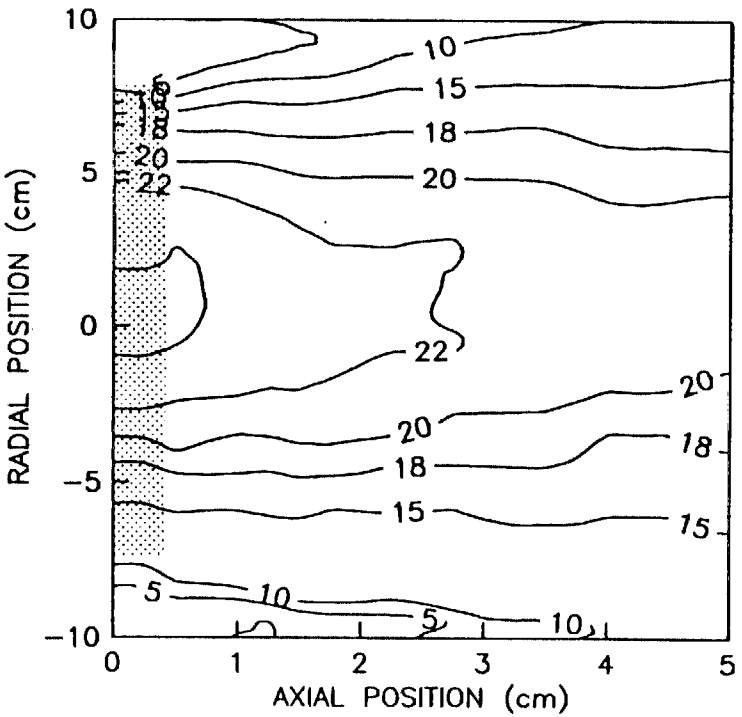

J_{id} = 2.1 mA
J_{iA} = 2.2 mA
J_{iV} = 0.17 mA

a) Neutralizer Operating
(J_N = 0.3 A, J_E = 230 mA)

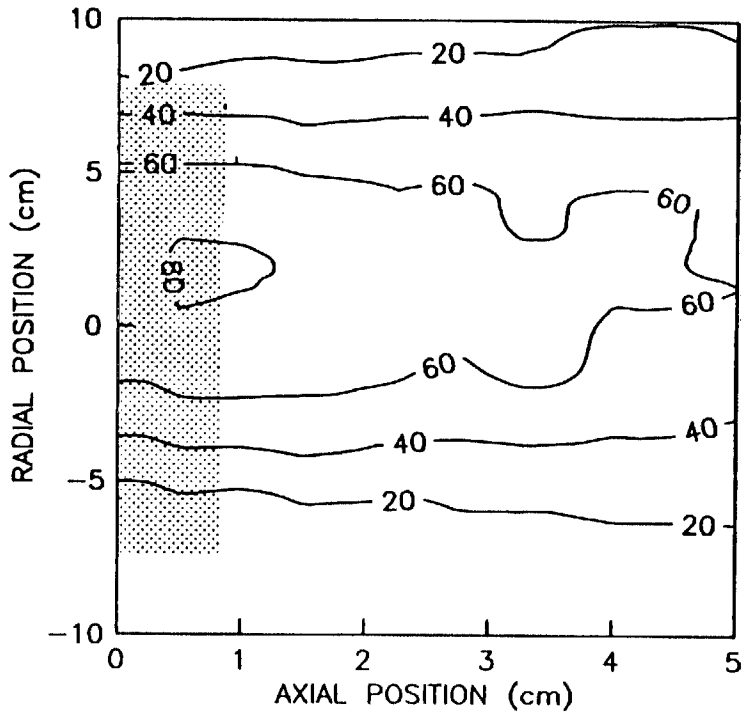

J_{id} = 2.1 mA
J_{iA} = 3.0 mA
J_{iV} = 0.30 mA

b) Neutralizer Discharge Off
(J_N = 0 A, J_E = 0 mA)

Fig. 12 Effects of Operating Without a Neutralizer

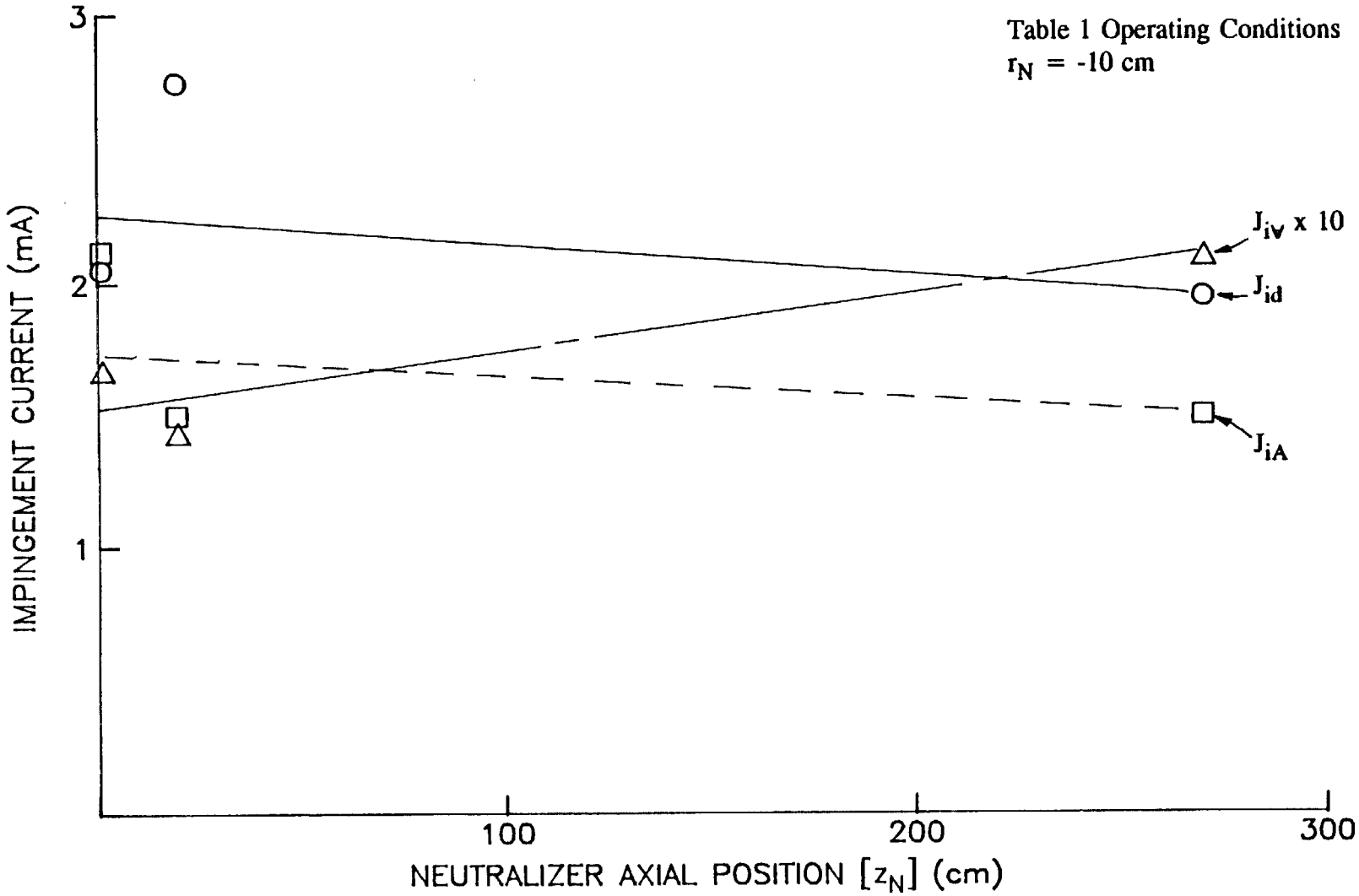

Fig. 13 Effects of Neutralizer Position on Impingement Currents

consistent correlation between neutralizer axial position and impingement current on the scale of the figure.

Finally, the effect of ambient background pressure, P_o, on impingement current determined using the three methods, was examined. The test was conducted by introducing additional xenon directly into the vacuum system while maintaining the flow rates into the ion thruster and the neutralizer. The data needed to construct ambient ion current density profiles, beam plasma potential maps and beam ion current density maps were measured and neutral density maps were computed as a function of ambient tank pressure. Impingement currents, determined as described previously, were found from these data and they are shown in Fig. 14 as a function of ambient tank pressure over the range from ~ 3 to 9 μTorr. The data in this figure show the expected increase in impingement current with ambient tank pressure. In addition, they continue to show relatively good agreement between the directly-measured and area-integrated impingement currents. The volume-integrated current, which has again been multiplied by ten, is, however, still an order magnitude below the corresponding directly measured and area-integrated values. The substantial decrease in the volume-integrated current at 9 μTorr was caused by a decrease in the charge-exchange ion extraction volume. This volume is difficult to determine accurately because the peak potential is generally located less than a centimeter from the accel grid. It is considered likely that volume-integrated impingement currents at 9 μTorr do not

Table 1 Operating Conditions

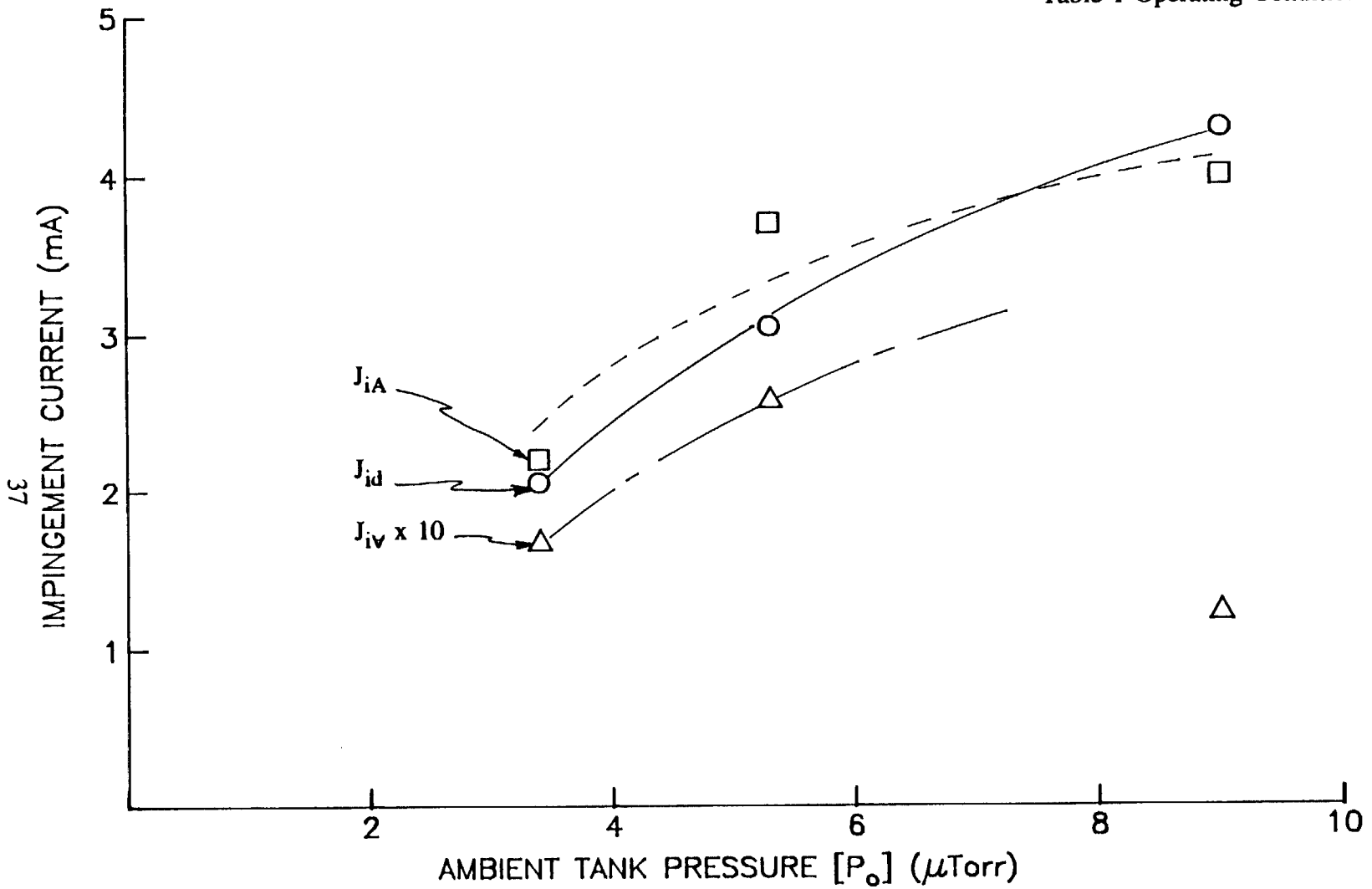

Fig. 14 Effects of Ambient Tank Pressure on Impingement Currents

follow the trend of the rest of the data because of an error related to the determination of this volume.

Discussion of Impingement Current Results

There are a number of possible sources of error that could be causing the order-of-magnitude differences that are consistently observed between the volume-integrated impingement currents and those measured directly and determined through area integration of the ambient ion current density. Some of these sources of error are much more likely to be important than others, but it is probably instructive at this point to consider all that can be identified. Such errors are reflected in the following list of possible deficiencies in the model or the measurements:

1. The basic assumption that the processes of charge-exchange ion production and ion attraction to the accel grid can be modelled in a gross sense may be invalid. It may be necessary to examine these processes on the scale of individual ion extraction holes and to then analyze data on this scale to determine the total impingement current.

2. If it is possible to examine the process on a scale that is large compared to the hole size, errors in the determination of the gross charge-exchange ion extraction volume applied herein are considered likely. Specifically, it is observed that the point of maximum beam potential, which is used as a boundary for determining the volume, is near the limit of resolution of the emissive probe technique being used to obtain it. This

boundary could be determined more accurately by using grids with larger hole diameters coupled possibly with a numerical technique for tracing the trajectories of charge-exchange ions that are produced throughout the region downstream of the accel grid. More accurate determination of the volume is not, however, expected to cause it to increase by the order of magnitude needed to bring the directly measured and volume-integrated impingement currents into agreement unless the tracing process is carried out on the scale of individual beamlets.

3. The assumption that charge-exchange ions are produced with zero kinetic energy is open to question. If these ions are created with substantial velocity components, they could overcome adverse potential gradients, thereby reaching the accel grid from further downstream. The ions could undergo upstream acceleration as a result of the charge-exchange reaction itself in which a beam ion overtaking a neutral could attract the neutral during the electron transfer process. Charge-exchange ions would also have upstream velocities if they were produced from neutrals that had significant upstream velocities before the reaction. Such neutrals might be formed as a consequence of ion impact on vacuum chamber surfaces. Both mechanisms should be examined further.

4. The assumption that the process of charge-exchange ion extraction is a steady one could be invalid. Measurements made during the course of this work show that potential fluctuations of order a few volts do occur in the

beam plasma. The extent to which these fluctuations affect the magnitude of the impingement current is not known, but one would expect the effect to be influenced more by the characteristics of power supplies than by a change from for mercury to xenon propellant. The effect is considered to be potentially significant and worthy of additional study.

5. Wake-induced errors associated with Faraday probe measurements used to obtain area-integrated impingement currents are considered likely, and the magnitudes of these errors need to be investigated further. If large errors do exist, the reason for the good agreement between area-integrated and directly-measured results must be understood.

Other errors that are considerably less likely to yield the order of magnitude changes that would be required to bring directly measured and volume integrated results into agreement include the following:

6. Charge-exchange cross sections could be in error, even through data from different researchers are in relatively good agreement [7].

7. Instrument mis-calibration could be causing errors in any measurement, but all instruments have been calibrated repeatedly during the testing.

8. Secondary electron emission from the accel grid could cause an error in the directly measured impingement current. The molybdenum grids used in the experiments have a low secondary electron emission coefficient and calculations suggest the error associated with this process should be less than a few percent. It is also possible that material with a higher secondary

electron emission coefficient has been sputtered onto the accel grid from the vacuum chamber, but this should still induce a small effect.

Conclusions

Experimental apparatus and procedures, developed during the current grant period, have been used to measure the accel grid impingement current of an ion thruster directly and to calculate it from other measured data. It has been shown that impingement currents can be calculated by integrating the ambient ion current density over the area of the accel grid, and by integrating the charge-exchange ion production rate over the charge-exchange ion extraction volume. Directly measured impingement currents agree with those determined by area integration of the ambient current density to within $\pm 50\%$. Impingement currents determined by volume-integration of the charge-exchange ion production rate are an order of magnitude less than these values. Additional effort is required to interpret fully the area-integrated impingement current data and to either develop a model based on volume-integration of charge-exchange ion production that agrees with directly measured impingement currents or to otherwise resolve the difference between them.

Preliminary test results obtained at low beam currents suggest turning the neutralizer off does not affect the impingement current significantly. The directly measured impingement current increases linearly with ambient tank pressure, as expected from both theoretical models and the experience of experimental researchers.

References

1. Staggs, J.F., W.P. Gula, Kerslake, W.R., " Distribution of Neutral Atoms and Ions Downstream of an Ion Thruster," Journal of Spacecraft and Rockets, Vol. 5, No. 2, Feb. 1968, pp. 159-164.

2. Peng, X., Keefer, D., and Ruyten, W., "Plasma Particle Simulation of Electrostatic Ion Thrusters," AIAA Paper 90-2647, July 1990, Orlando, FL.

3. Rawlin, V.K., "Internal Erosion Rates of a 10-kW Xenon Ion Thruster," AIAA Paper 88-2912, July 1988, Boston, MA.

4. Byers, D.C. and Staggs, J.F., "SERT II Flight-Type Thruster System Performance," AIAA Paper 69-235, March 1969, Williamsburg, VA.

5. Wilbur, P.J., "Modified SERT II Ion Thruster Operation on Xenon," Appears in "Advanced Electric Propulsion Research," NASA CR-182130, Jan. 1988, pp. 53-63.

6. Kerslake, W. K.,"Charge Exchange Effects on the Accelerator Impingement of an Electron-Bombardment Ion Rocket," NASA TN D-1657, May, 1963.

7. Rapp, D. and Francis, W. E., "Charge Exchange between Gaseous Ions and Atoms," The Journal of Chemical Physics, Vol. 37, No. 11, Dec. 1962, pp. 2631-2645.

8. Anon.,"Surfer, Version 4 Reference Manual,", Golden Software, Inc. Golden, Co.

9. Rawlin, V.K. and Kerslake, W.R., "Durability of SERT II Hollow Cathode and Future Applications of Hollow Cathodes," AIAA Paper 69-304, March 1969, Williamsburg, VA.

10. Stone N. H., "The Aerodynamics of Bodies in a Rarefied Ionized Gas With Application to Spacecraft Environmental Dynamics", NASA Technical Paper 1933, Nov. 1981.

11. Lee, Sears and Turcotte, Statistical Thermodynamics 2nd Ed., Addison Wesley, 1973

12. Collett, C. et al, "Thruster Endurance Test," NASA CR-135011, May 1976, pp 195-197.

APPENDIX A

A Model of the Molecular Density Downstream of an Accel Grid

The neutral density throughout the region downstream of the accel grid of an ion thruster can be computed numerically using a free-molecular-flow model of the process. The accel grid is modeled as a multi-hole, thin, planar plate through which neutrals flow at a prescribed rate into a region that is at a prescribed density far downstream of the plate. The analysis involves the development of an expression for the neutral density at any point downstream of a single hole. This expression is then applied repeatedly to sum the contributions of each hole in the plate at all downstream points. Finally, the background density of the neutrals is added to the density due to flow through the grids to obtain the total density at any location.

The expression for the neutral density distribution downstream of a hole in a plate separating a region into which gas is supplied from a low pressure downstream region is developed considering the physical arrangement of Fig. A1. In order to simplify the analysis, it is assumed that: 1) the neutrals, which are present within the source region at a uniform density n_s, are in equilibrium with the walls of the supply chamber at a temperature T_w, 2) the mean free path for collisions between molecules is large compared with the diameter of the hole, 3) the plate is sufficiently thin so that essentially none of the molecules collide with the barrel of the hole, 4) the downstream region is sufficiently well-pumped so the effect of molecules that backflow from the downstream region into the thruster

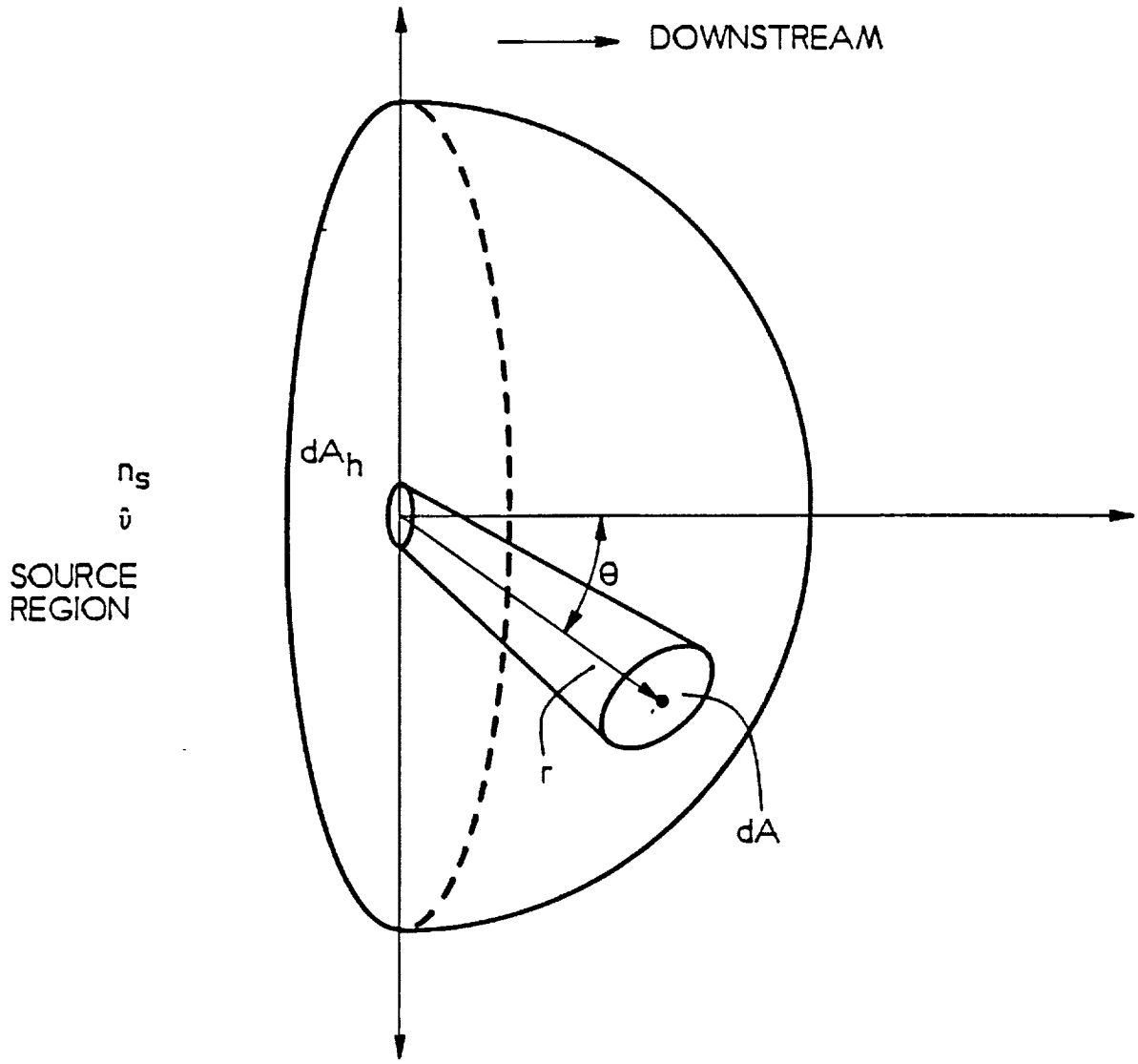

Fig. A1 Physical Arrangement Used for Neutral Density Model Development

through the grids can be neglected (i.e. the neutral density within the test chamber is substantially less than that in the thruster) and 5) the region of interest is sufficiently far downstream so that each hole in the plate can be treated as a point source.

A portion of the neutrals with mass m that pass through a region of the hole in the plate with differential area dA_h will exit at an angle θ from the normal to the plate and will pass through a differential solid angle $d\omega$ in the manner suggested in Fig. A1. Their flow rate per differential solid angle per unit of differential hole area is given by [11]

$$\frac{d^2 \dot{N}_s}{d\omega \, dA_h} = \frac{1}{4\pi} n_s \, \hat{v}_s \cos(\theta) \quad , \tag{A1}$$

where

$$\hat{v}_s = \frac{1}{4} \sqrt{\frac{8kT_w}{\pi m}}$$

is the mean thermal speed of these neutrals in any prescribed direction. Assuming the atoms have no atom-atom momentum transfer collisions once they leave the hole, they will pass through the differential area dA on a hemisphere centered on the hole with a mean velocity $\hat{v} = \hat{v}_s$ at a differential rate $d\dot{N} = d\dot{N}_s$. Hence at this location, the differential flow rate per unit solid angle per unit of hole area will be

$$\frac{d^2 \dot{N}}{d\omega \, dA_h} = \frac{1}{4\pi} n_s \hat{v} \cos(\theta) \quad . \tag{A2}$$

Applying the definition of solid angle

$$d\omega = \frac{dA}{r^2} \quad , \tag{A3}$$

Eq. A2 can be rewritten to obtain

$$\frac{d^2\dot{N}}{dA\, dA_h} = \frac{1}{4\pi} \frac{n_s \hat{v} \cos(\theta)}{r^2} \quad . \tag{A4}$$

Assuming the distance r is sufficiently great so that the angle θ between the normal to the source hole and the line between any point on that hole and the differential area dA are about equal, Eq. A4 can be integrated over the hole area, A_h, to obtain

$$\frac{d\dot{N}}{dA} = \frac{1}{4\pi} \frac{A_h n_s \hat{v} \cos(\theta)}{r^2} \quad . \tag{A5}$$

The differential neutral flow rate through the differential area dA is given by

$$\frac{d\dot{N}}{dA} = n\hat{v} \quad , \tag{A6}$$

where n is the neutral density at the differential area, dA, due to flow through the hole. Equations A5 and A6 are combined to obtain the following expression for the atomic density n at a point on a spherical surface a distance r and at an angle θ

from a plane normal to a hole with area A_h where the density is n_s.

$$n = \frac{A_h n_s \cos(\theta)}{4\pi r^2} \quad . \tag{A7}$$

Since the atomic flow rate through the hole $\dot{N}_h$ is related to the density at the hole by the equation

$$\dot{N} = n_s A_h \hat{v} \quad . \tag{A8}$$

Eq. A7 can be rewritten

$$n = \frac{\dot{N}_h \cos(\theta)}{4\pi r^2 \hat{v}} \quad . \tag{A9}$$

Using this expression for the neutral density distribution downstream of a single hole, the effect of flows through multiple holes on the density at a prescribed downstream point "i" can be found by summing the contributions from each hole. In order to do this, the accel grid is assumed planar and neutral densities are calculated at points on a plane that is normal to the grid plane and contains the thruster centerline as shown in Fig. A2. As the figure suggests, the neutral density contributions due to holes in half of the grid are summed, and symmetry is invoked to account for flow from the other half.

As Fig. A2 suggests, the distance r between the j^{th} hole located at

$[x_{h,j}, y_{h,j}, 0]$ on the accel grid and the i^{th} point located at $[x_{p,i}, 0, z_{p,i}]$ on the calculation plane is given by

$$r = [(x_{h,j} - x_{p,i})^2 + y_{h,j}^2 + z_{p,i}^2]^{1/2} \quad . \tag{A10}$$

In addition, Fig. A2 shows that the cosine of the angle between the normal to the hole and the radius vector r (i.e. $\cos(\theta)$) is given by

$$\cos(\theta) = \frac{z_{p,i}}{r} = \frac{z_{p,i}}{[(x_{h,j} - x_{p,i})^2 + y_{h,j}^2 + z_{p,i}^2]^{1/2}} \quad . \tag{A11}$$

Substituting Eqs. (A10) and (A11) into Eq. (A9) one obtains the following expression for the density at point i due to flow from the j^{th} hole

$$n_j(x_{p,i}, z_{p,i}) = \frac{\dot{N}_h}{4\pi\hat{v}} \frac{z_{p,i}}{\left[(x_{h,j} - x_{p,i})^2 + y_{h,j}^2 + z_{p,i}^2\right]^{\frac{3}{2}}} \quad . \tag{A12}$$

This expression can be used to obtain the total neutral density at point "i" downstream of the accel grid by summing the density contributions from each of the holes in the accel half-grid and multiplying the result by a symmetry factor γ_j. This symmetry factor is 2 for all of the holes but those at y=0. The symmetry factor for holes at y=0 is 1 because the plane bisects these holes. The density at any point "i" due to flow through n_h holes is computed numerically using

$$n(x_{p,i}, x_{p,i}) = \frac{\dot{N}_h}{4\pi\hat{v}} \sum_{j=1}^{n_h} \frac{\gamma_j \, z_{p,i}}{\left[(x_{h,j} - x_{p,i})^2 + y_{h,j}^2 + z_{p,i}^2\right]^{\frac{3}{2}}} \quad . \tag{A12}$$

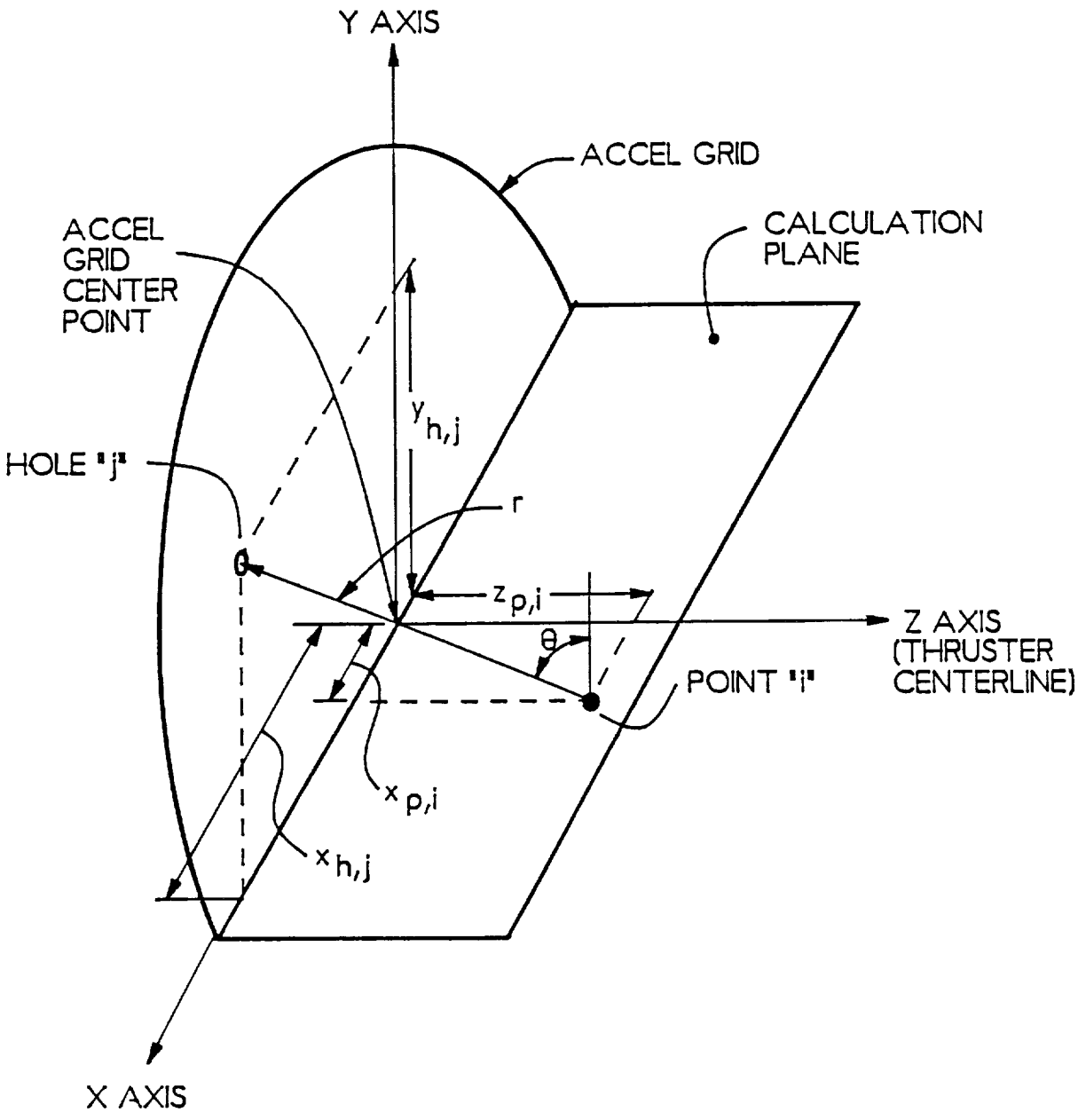

Fig. A2 Multiple Hole Neutral Density Calculation Geometry

The true density must additionally reflect the contribution of the ambient neutral density that exists in the vacuum tank at locations far from the thruster. This density, which is determined by the ambient tank pressure, P_o, and the tank wall temperature, T_o, through the perfect gas equation, must be added to the results of Eq. A13 obtain the following final result.

$$n(x_{p,i}, x_{p,i}) = \frac{\dot{N}_h}{4\pi\bar{v}} \sum_{j=1}^{n_h} \frac{\gamma_j \, z_{p,i}}{\left[(x_{h,j} - x_{p,i})^2 + y_{h,j}^2 + z_{p,i}^2\right]^{\frac{3}{2}}} + \frac{P_o}{kT_o} \quad . \qquad (A14)$$

The significance of each of the terms in the above equation can be seen by applying it to a typical thruster and typical propellants. For the operating conditions of Table 1, the first and second terms in Eq. A14 yield densities of the order $2x10^{11}$ cm^{-3} and $1x10^{11}$ cm^{-3}, respectively, for xenon and for the higher flow rates of mercury the densities are and $4x10^{11}$ cm^{-3} and $1x10^{11}$ cm^{-3}, respectively.

DISTRIBUTION LIST

	Copies
National Aeronautics and Space Administration Washington, DC 20546 Attn:	
RP/Mr. Earl E. VanLaningham, MS B600	1
RP/Mr. Gary Bennett, MS B600	1
RP/Mr. Marcus Watkins, MS B600	1
National Aeronautics and Space Administration Lewis Research Center 21000 Brookpark Road Cleveland, OH 44135 Attn:	
Technology Utilization Office, MS 7-3	1
Report Control Office, MS 60-1	1
Library, MS 60-3	2
Dr. M. Goldstein, Chief Scientist, MS 5-9	1
Mr. Dave Byers, MS 500-219	1
Mr. Jim Stone, MS 501-6	1
Mr. Vincent Rawlin, MS 500-219	10
Mr. Bruce Banks, MS 302-1	1
Mr. Michael Patterson, MS 500-219	1
Mr. Tim Verhey, MS 500-219	1
Mr. Jim Sovey, MS 500-219	1
National Aeronautics and Space Administration Marshall Space Flight Center Huntsville, AL 35812 Attn:	
Mr. Ralph Carruth, Mail Code ES 53	1
Mr. Jason Vaughn, Mail Code ES 53	1
NASA Scientific and Technical Information Facility P.O. Box 8757 Baltimore, MD 21240 Attn:	
Accessioning Dept.	1

	Copies
Dept. of the Navy Office of Naval Research Universiy of New Mexico Bandolier Hall West Albuquerque, NM 87131 Attn: G. Max Irving	1
Case Western Reserve University 10900 Euclid Avenue Cleveland, OH 44106 Attn: Dr. Eli Reshotko	1
Procurement Executive, Ministry of Defense Royal Aircraft Extablishment Farnborough, Hants GU14 6TD ENGLAND Attn: Dr. D. G. Fearn	1
United Kingdom Atomic Energy Authority Culham Laboratory Abingdon, Oxfordshire OX143DB ENGLAND Attn: Dr. A. R. Martin (Rm F4/135)	1
Intelsat 3400 International Dr. N.W. Washington D.C. 20008-3098 Attn: Mr. Bernard Free, MS 33	1
Air Force Astronautics Lab Edwards AFB, CA 93523-5000 Attn: LKDH/Lt. Phil Roberts, MS 24 LSVE/Mr. J. Chris Andrews PL/VSA/Dr. Robert Vondra	1 1 1

	Copies
Giessen University lst Institute of Physics Giessen, West Germany Attn:	
Professor H. W. Loeb	1
Jet Propulsion Laboratory 4800 Oak Grove Laboratory Pasadena, CA 91109 Attn:	
Technical Library	1
Dr. John Barnett, MS 125-224	1
Dr. John Brophy, MS 125-224	1
Dr. Charles Garner, MS 125-224	1
TRW Inc. TRW Systems One Space Park Redondo Beach, CA 90278 Attn:	
Mr. Sid Zafran	1
National Aeronautics and Space Administration Ames Research Center Moffett Field, CA 94035 Attn:	
Technical Library	1
National Aeronautics and Space Administration Langley Research Center Langley Field Station Hampton, VA 23365 Attn:	
Technical Library	1
Hughes Research Laboratories 3011 Malibu Canyon Road Malibu, CA 90265 Attn:	
Dr. Jay Hyman, MS RL 57	1
Dr. J. R. Beattie, MS RL 57	1
Dr. J. N. Matossian, MS RL 57	1

	Copies
Engineering Quadrangle Princeton University Princeton, NJ 08540 Attn:	
Prof R. G. Jahn	1
Dr. Arnold Kelly	1
Boeing Aerospace Co. P. O. Box 3999 Seattle, WA 98124-2499 Attn:	
Dr. J.S. Meserole, MS 82/83	1
Rocket Research Co. P.O. Box 97009 Redmond, WA 98073-9709 Attn:	
Mr. William W. Smith	1
Mr. Paul Lichon	1
Dr. Dave King	1
Electrotechnical Laboratory 1-1-4, Umezono, Tsukuba-Shi Ibaraki, 305 JAPAN Attn:	
Dr. Isao Kudo	1
Sandia Laboratories P. O. Box 5800 Albuquerque, NM 87185 Attn:	
Mr. Ralph R. Peters, Mail Code 4537	1
Mr. Dean Rovang, Mail Code 1251	1
Ion Tech Inc. 2330 E. Prospect Road Fort Collins, CO 80525 Attn:	
Dr. Gerald C. Isaacson	1
Dr. Dan Siegfried	1
Mr. Larry Daniels	1

	Copies
EG & G Idaho P. O. Box 1625 Idaho Falls, ID 83401 Attn: Dr. G. R. Longhurst, TSA-104	1
Michigan State University East Lansing, MI 48824 Attn: Dr. J. Asmussen Dr. M.C. Hawley	1 1
Aerospace Engineering Department Faculty of Engineering Tokai University Kitakanome, Hiratsuka-shi, Kanagawa-ken, JAPAN 259 Attn: Prof. Itsuro Kimura	1
Department of Electronics Tokyo National Technical College No. 1220-2 Kunugida-cha, Hachioji 193 Tokyo, JAPAN Attn: Mr. Susumu Masaki	1
Tuskegee Institute School of Engineering Tuskegee Institute, AL 36088 Attn: Dr. Pradosh Ray	1
Mr. Lee Parker 252 Lexington Road Concord, MA 01741	1

Copies

Physics Department
Naval Postgraduate School
Monterey, CA 93943-5000
Attn:
Dr. Chris Olson, Mail Code 61-0S 1

Martin Marietta Aerospace
P. O. Box 179
Denver, CO 80201
Attn:
Dr. Kevin Rudolph, MS M0482 1

S-Cubed
P. O. Box 1620
LaJolla, CA 92038
Attn:
Dr. Ira Katz 1

Dept. of Aero. & Astro. Eng.
101 Transportation Bldg.
104 South Mathews Ave.
Urbane, IL 61801-2997
Attn:
Dr. Rodney Burton 1

Teletronix Inc.
P.O. Box 500
Beaverton, OR 97077
Attn:
Mr. Curtis Haynes, MS 50-324 1

W. J. Schafer Assoc. Inc.
1901 North Fort Meyer Dr., Suite No. 800
Arlington, VA 22209
Attn:
Dr. Herbert Cohen 1

Electric Propulsion Laboratory, Inc.
440 N. Green St.
Tehachapi, CA 93561
Attn:
Dr. Graeme Aston 1

Copies

Department of Aeronautics
University of Tokyo
7-3-1 Hongo, Bunko-ku
Tokyo 113, Japan
Attn:
Prof. Yoshihiro Arakawa 1

National Space Development Agency of Japan
2-4-1 Humamatsu-cho, Minato-ku
Tokyo 105, Japan
Attn:
Mr. Kenichi Kajiwara 1
Propulsion Engineering Group 1
Launch Vehicle Dept. 1

National Aerospace Laboratory
7-44-1 Jindiajigashi-machi, Chofu
Tokyo 182, Japan
Attn:
Mr. Yukio Hayakawa 1

Center for Aerospace Research
University of Tennessee Space Institute
Tullahoma, TN 37388-8897
Attn:
Mr. Verlin Friedly 1